# Argonne National Laboratory

## A STUDY OF THE PHYSICAL PROPERTIES OF NOMINAL 0.7, 3, AND 6 a/o BURNUP UO$_2$ FAST-REACTOR FUEL PINS PREPARATORY TO TRANSIENT TREAT EXPOSURE

by

R. R. Stewart, C. E. Dickerman,
N. R. Stalica, and W. B. Doe

The facilities of Argonne National Laboratory are owned by the United States Government. Under the terms of a contract (W-31-109-Eng-38) between the U. S. Atomic Energy Commission, Argonne Universities Association and The University of Chicago, the University employs the staff and operates the Laboratory in accordance with policies and programs formulated, approved and reviewed by the Association.

ARGONNE NATIONAL LABORATORY
9700 South Cass Avenue
Argonne, Illinois 60439

# A STUDY OF THE PHYSICAL PROPERTIES OF NOMINAL 0.7, 3, AND 6 a/o BURNUP UO₂ FAST-REACTOR FUEL PINS PREPARATORY TO TRANSIENT TREAT EXPOSURE

A STUDY OF THE PHYSICAL PROPERTIES OF
NOMINAL 0.7, 3, AND 6 a/o BURNUP
UO₂ FAST-REACTOR FUEL PINS
PREPARATORY TO TRANSIENT TREAT EXPOSURE

by

R. R. Stewart, C. E. Dickerman,
Reactor Physics Division

N. R. Stalica,
Chemical Engineering Division

and

W. B. Doe
Reactor Operations Division

May 1969

# TABLE OF CONTENTS

4

## LIST OF FIGURES

## LIST OF FIGURES

## LIST OF FIGURES

## LIST OF TABLES

# A STUDY OF THE PHYSICAL PROPERTIES OF
# NOMINAL 0.7, 3, and 6 a/o BURNUP
# UO$_2$ FAST-REACTOR FUEL PINS
# PREPARATORY TO TRANSIENT TREAT EXPOSURE

by

R. R. Stewart, C. E. Dickerman,
N. R. Stalica, and W. B. Doe

## ABSTRACT

A need for the characterization of the physical condition of 0.7, 3.0, and 6.0 a/o burnup UO$_2$ fast-reactor fuel pins prompted this detailed study. The information gained from this study is documented by numerous charts, tables, neutron and X-ray radiographs, photographs, photomicrographs, and beta-gamma and alpha radiographs, all of which may be used as a comparison for future studies involving uranium oxides or mixed plutonium-uranium oxides.

Solid and gaseous fission products are generated during steady-state irradiation of UO$_2$. Some of these fission products are retained within the UO$_2$ matrix, causing changes in the physicochemical composition and dimensional stability of the fuel. These effects are discussed.

Five fuel pins were used for destructive examination, as many as 18 separate samples being examined from one pin. These five pins were representative of the 0.7, 3.0, and 6.0 a/o burnup groups, which had been irradiated at an initial power density of 2.5 kW/cc, corresponding to initial fuel centerline and fuel surface temperatures of 2400 and 1215°C, respectively.

Extensive studies were made on several pin cross sections from each burnup group using an electron-microprobe analyzer. As a result of these studies, the microstructural appearance of the fuel has been brought into full focus.

An especially interesting phenomenon was the occurrence of metallic inclusions, which were found predominantly within large porous regions at the fuel periphery and contained the transition metal fission products molybdenum, ruthenium, technetium, rhodium, and palladium. The studies of this phenomenon along with the studies of fission-product concentrations and distributions are presented and discussed.

# I. INTRODUCTION

Steady-state irradiation of gas-bonded uranium dioxide fast-reactor type fuel pins produces fission products, some of which are retained within the structure of the $UO_2$, and also produces changes in the fuel geometry, structure, and physicochemical composition. The fission products that are generated during the irradiation process are found in both gaseous and solid forms.

The purpose of this study was to characterize the physical condition of a group of such pins after steady-state irradiation to burnup in the approximate range 0.7-6 a/o, preparatory to running selected pins from that group in fast-reactor safety experiments in the Transient Reactor Test (TREAT) Facility.

An experimental program[1] is under way, using the TREAT reactor, to study modes of fuel-pin failure, changes in fuel during temperature excursions, fuel motion arising from failure, pressure generation associated with failure, coolant movement arising from failure, and a broad range of possible postfailure phenomena that could propagate and cause a super-prompt-critical secondary accident.

Twenty steel-clad, gas-bonded EBR-II type fuel pins were irradiated in the Materials Testing Reactor (MTR) to nominal burnups of 0.7, 3.0, and 6.0 a/o. A preliminary report has been issued on the postirradiation condition of the lower-burnup (0.7 and 3.0 a/o nominal burnup levels) pins.[2] A separate report has been issued on the postirradiation condition of the higher-burnup (6.0 a/o level) pins.[3]

Five of the irradiated pins were tested in TREAT transient experiments: a summary of the results from the first four has been reported;[4] a summary of the fifth is reported[5] separately.

Complete results of the TREAT experiments on irradiated oxide pins from the group described in this report are published as a sister report,[6] and should be consulted for information pertinent to the transient experiments.

## II.  FUEL CONDITION AFTER STEADY-STATE IRRADIATION

### A.  Fuel Samples

Twenty gas-bonded, half-length EBR-II Mark-I-like $UO_2$ pins were made for the steady-state irradiation.  Each pin consisted of a 14.5-cm-long stack of 13% enriched $UO_2$ cylinders, 0.381 cm in diameter, argon-bonded to a Type 304 stainless steel jacket of 0.396-cm ID and 0.442-cm OD.

The fuel cylinders were made by the Metallurgy Division Ceramics Group.  Ceramic-grade Kerr-McGee oxide powder of natural enrichment, with a particle size of $0.5\,\mu$ and surface area of 10 $m^2$ per gram, was blended with fully enriched oxide to provide the specified enrichment of 13%. The particle size of the enriched oxide was equal to or greater than $2$-$3\,\mu$ after milling. (Size before milling was $44\,\mu$.)  This powder was mixed with $2$-$2\frac{1}{2}$% methylcellulose to form a slurry and then dried out, after which 10-15% $H_2O$ was added and mixed thoroughly with the slurry.  After the slurry was extruded under a 5-7-ton load, the green density was 40% of theoretical density.  The extrusions were then cut into lengths and sintered at 1700-1750°C for 4 hr.[7]  The resultant density varied from 91.05 to 94.73% of theoretical density, with an average density of 92.07% of theoretical density.*

Using data obtained from fuel analyses, shown in Table I (oxygen)[9] and in Table II (uranium),[10] we calculated the ratio of oxygen to uranium to be $2.019 \pm 0.008$.  The molecular weight of the uranium was taken from the manufacturer's isotopic analysis of the uranium fuel, which appears in Table III.[7]  To check the degree of homogeneity in the fuel, we obtained further data from ANL isotopic analyses of randomly chosen fuel samples, the results of which appear in Table IV.[11]  The calculated molecular weights of the uranium for the different analyses were all approximately 237.6, which yielded the final oxygen-to-uranium ratio of 2.019.  Table V is the spectro-chemical analyses of fuel impurities for the final blended oxide of 13% enrichment.[12]

| TABLE I.  Results of Chemical Analysis for Oxygen (Batch No. 2-2-1708) | |
|---|---|
| Sample No. | Oxygen, % |
| 1 | 12.08 ± 0.048 |
| 2 | 12.02 ± 0.048 |

| TABLE II.  Results of Chemical Analysis for Uranium (Batch No. 2-2-1708) | | |
|---|---|---|
| Sample No. | Uranium, % | |
| 1 | 88.75 | 88.59 ± 0.16 |
| 2 | 88.43 | |

---

*Theoretical density of 10.96 g/cc (obtained by X-ray measurement) from Ref. 8.

TABLE III. Results of Manufacturer's Isotopic Analysis
of the Uranium Fuel (Batch No. 2-2-1708)

| Mass | Ratio | Mole Percent | Weight Percent | Precision Sigma |
|------|-------|--------------|----------------|-----------------|
| 234 | 0.0015272 | 0.132325 | 0.130321 | 0.000728 |
| 235 | 0.1520600 | 13.174700 | 13.030618 | 0.030956 |
| 236 | 0.0005976 | 0.051780 | 0.051431 | 0.000707 |
| 238 | 0.9999976 | 86.641202 | 86.787630 | 0.030902 |

TABLE IV. Results of ANL Isotopic Analyses of Uranium
Fuel Samples[a] (Batch No. 2-2-1708)

| Mass | Isotopic Composition, a/o | | |
|------|---------------------------|---|---|
| | $M_1$, Definite Control | $M_2$, Same Batch | $M_3$, Same Batch |
| 234 | 0.134 | 0.127 | 0.137 |
| 235 | 13.29 ± 0.02 | 13.08 ± 0.02 | 13.50 ± 0.03 |
| 236 | 0.056 | 0.047 | 0.053 |
| 238 | 86.52 ± 0.02 | 86.75 ± 0.02 | 86.31 ± 0.02 |

[a]The isotopic analysis of $M_1$ is considered representative of the starting
material. $M_2$ and $M_3$ are samples from the same batch of nominally
identical material. All three samples were analyzed consecutively on
the same mass spectrometer for isotopic composition.

TABLE V. Results of Spectrochemical Analyses of Fuel Impurities

| Element | Level, ppm | Element | Level, ppm |
|---------|-----------|---------|-----------|
| Ag | <1 | Mg | 8 |
| Al | 150 | Mn | <1 |
| As | <20 | Mo | 20 |
| B | 0.2 | Na | 5 |
| Be | <0.5 | Ni | 50 |
| Bi | <1 | P | <100 |
| Ca | <50 | Pb | 1 (?) |
| Co | <5 | Sb | <10 |
| Cr | 40 | Si | 50 |
| Cu | 2 | Sn | 5 |
| Fe | 800 | Ti | 100 |
| K | <50 | Zn | <50 |
| Li | <5 | | |

475 μ
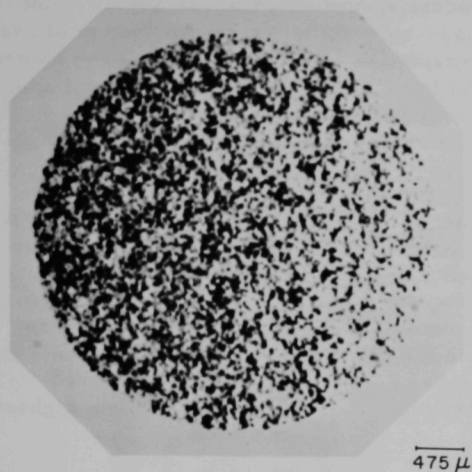
112-8893

Fig. 1. Beta-Gamma Autoradiograph of a Sample Prepared from Original UO$_2$ Material as a Control Specimen

Figure 1 is a beta-gamma autoradiograph of a control sample exposed to fine-grain positive film for 72 hr, developed in a high-contact developing solution and enlarged. This photomicrograph clearly shows the non-homogeneity of the initial starting fuel.

Standard EBR-II cladding tubes and end fittings were used. Inside the cladding, a space approximately 5.7 cm long extended above the fuel to provide a gas plenum for fission gases released during the steady-state exposure. Each pin had a standard 0.12-cm-diam EBR-II stainless steel spacer wire wrapped around the cladding in a spiral. An aluminum 0.1 w/o cobalt-alloy neutron-flux monitor wire was also wrapped around each sample. The pins were then sodium bonded in standard MTR irradiation capsules designed for full-length EBR-II-size pins,[13] two of the half-length oxide pins to a capsule.

Design power at the beginning of the steady-state irradiation was 2.5 kW/cc. Calculated centerline and fuel-surface temperatures at this power density are 2400 and 1215°C, respectively. Six pins (1-6) were programmed for burnup of approximately 0.7 a/o and were irradiated for 30 days; eight pins (7-14) had a target burnup of 3 a/o and were irradiated for 123 days; the remaining six pins (15-20) were run for 273 days to attain a nominal 6 a/o burnup. The thermal-flux depression was not excessive. Under "average" irradiation conditions (that is, for 3 a/o burnup), the ratio of radial maximum power to average power was estimated to be 1.1, corresponding to a radial-flux depression of about 17%.

After irradiation in MTR, the capsules were returned to the ANL Hot Laboratories in Illinois for disassembly and inspection of the pins, and subsequent reencapsulation for transient irradiation experiments in the TREAT reactor.

Inspection procedures included photography of the condition of the pins, checks on dimension changes, axial gamma scanning, neutron radiographs[14] made using a thermal-neutron beam from the Juggernaut reactor, X-ray photographs, and burnup determinations by radiochemical analyses of the monitor wires. Five pins were set aside as control specimens to be

given destructive examinations, including collection of released fission gases, burnup measurement by mass-spectrometric determination of uranium isotopic ratios, and ceramographic examinations. Two of the control specimens were of 0.7 a/o nominal burnup, two were nominally of 3 a/o, and the remaining pin was from the highest-burnup group.

## B. Macroscopic Examinations

Figure 2 shows the condition of odd-numbered pins 1-13 after removal from their MTR capsules. Spiral wires welded to the samples are the spacers; the smaller wires tied to the pins are the monitor wires. Although some cladding-surface discoloration and monitor-wire deterioration are apparent, the pins were sound. Steady-state irradiations were performed with pin 2 above pin 1 in the first capsule, pin 4 above pin 3 in the second capsule, and so on. Figure 2 is typical of even-numbered pins 2-14. Figure 3 shows the postirradiation condition of the six highest-burnup pins.

The identifying number of each pin is indicated at the bottom of each figure. Although surface discoloration is apparent on each pin, this is only external and is not indicative of any diametral changes. In fact, the average steel-jacket OD was still 0.174 in. (0.442 cm) as measured twice at half-inch intervals, one measurement being 90° to the other, over the entire length of the pin.

The dark discoloration appearing on each pin approximately two-thirds the way up from the spade end is believed to be the result of a "plating out" of sodium impurities in a region of temperature transition to the cooler cladding at the pin plenum. Spectrographic analyses of the material showed iron, chromium, nickel, tin, and aluminum to be major constituents.

No metallographic evidence was found for cladding defects in this region. The 6 a/o burnup pin run in TREAT failed in this region.*

The pins were gamma-scanned after a five-month "cooling" period. Figures 4 and 5 show the results of axial scans of gross gamma activity; Fig. 4 shows gamma scans for pins 1-14; Fig. 5 shows those for the 6 a/o burnup pins. Sharp drops in counting rates caused by axial gaps in the oxide stacks are prominent. Although axial gradients in activity occur, there is no evidence for gross axial fuel motion or segregation of fission products.

Samples for radiochemistry were taken from the monitor wires at the top, middle, and bottom of each pin. In addition, segments of oxide from the central region of the five pins given destructive examinations were

---

*See Section III.B (Results of Transient Experiments of Ref. 6).
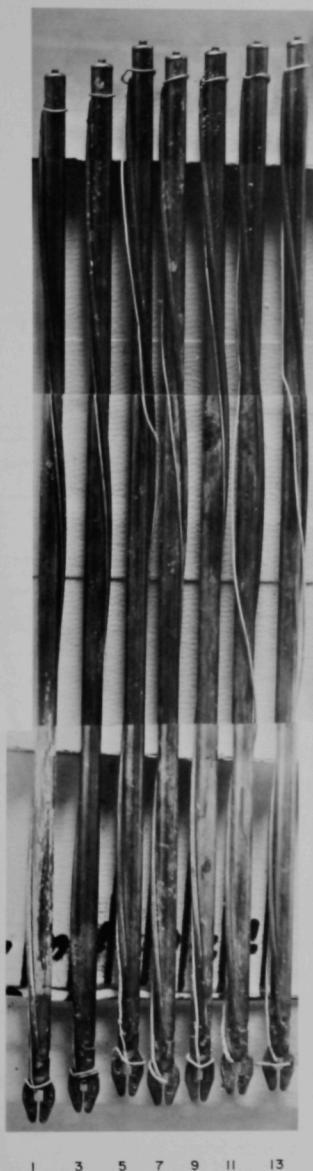
112-7439

Fig. 2. Postirradiation Condition of
Odd-numbered Pins 1-13,
before Remote Removal of
Flux Monitor Wires
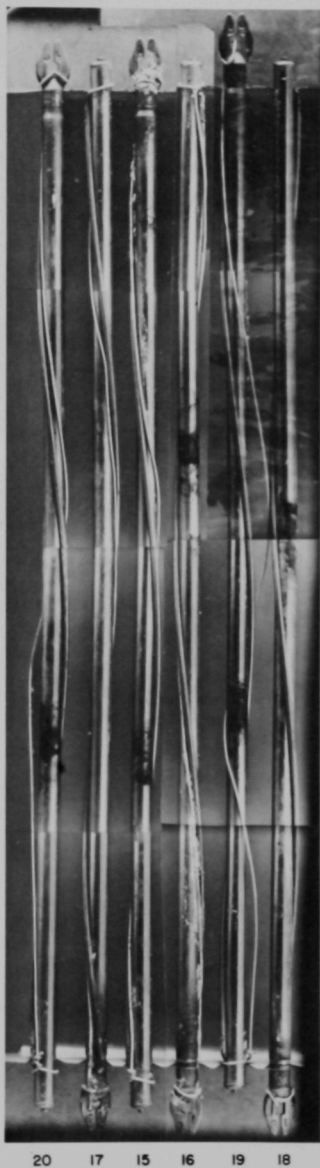


112-8623

Fig. 3. Postirradiation Condition of
Pins 15-20, before Remote Re-
moval of Flux Monitor Wires

16
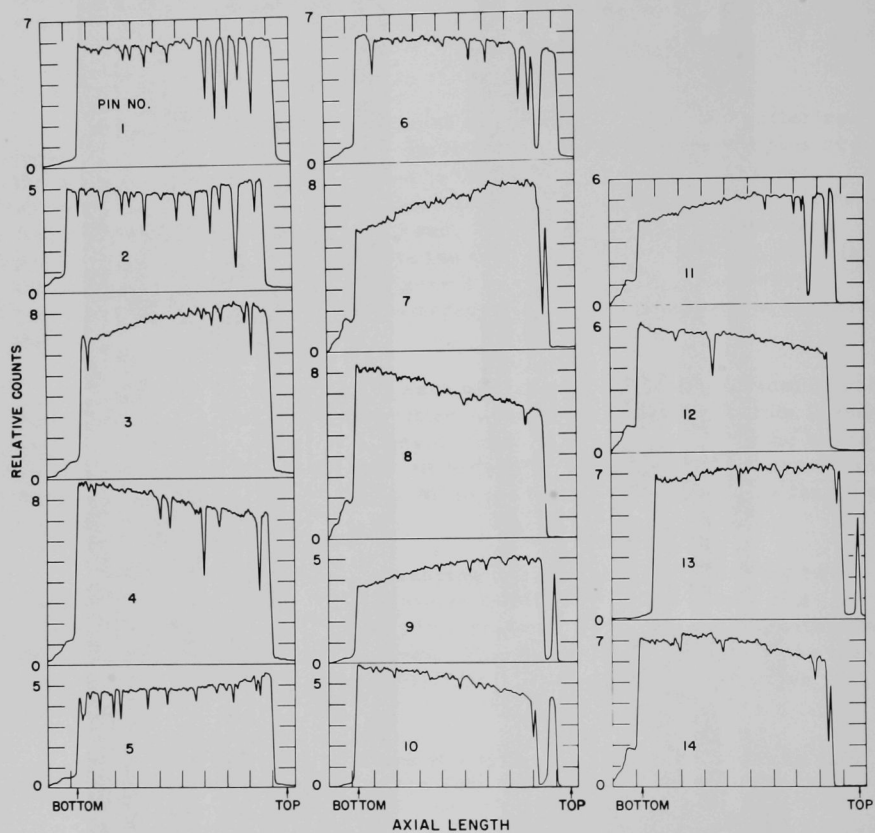


112-7366 Rev. 1

Fig. 4.  Axial Gamma-ray Scan Data for Pins 1-14
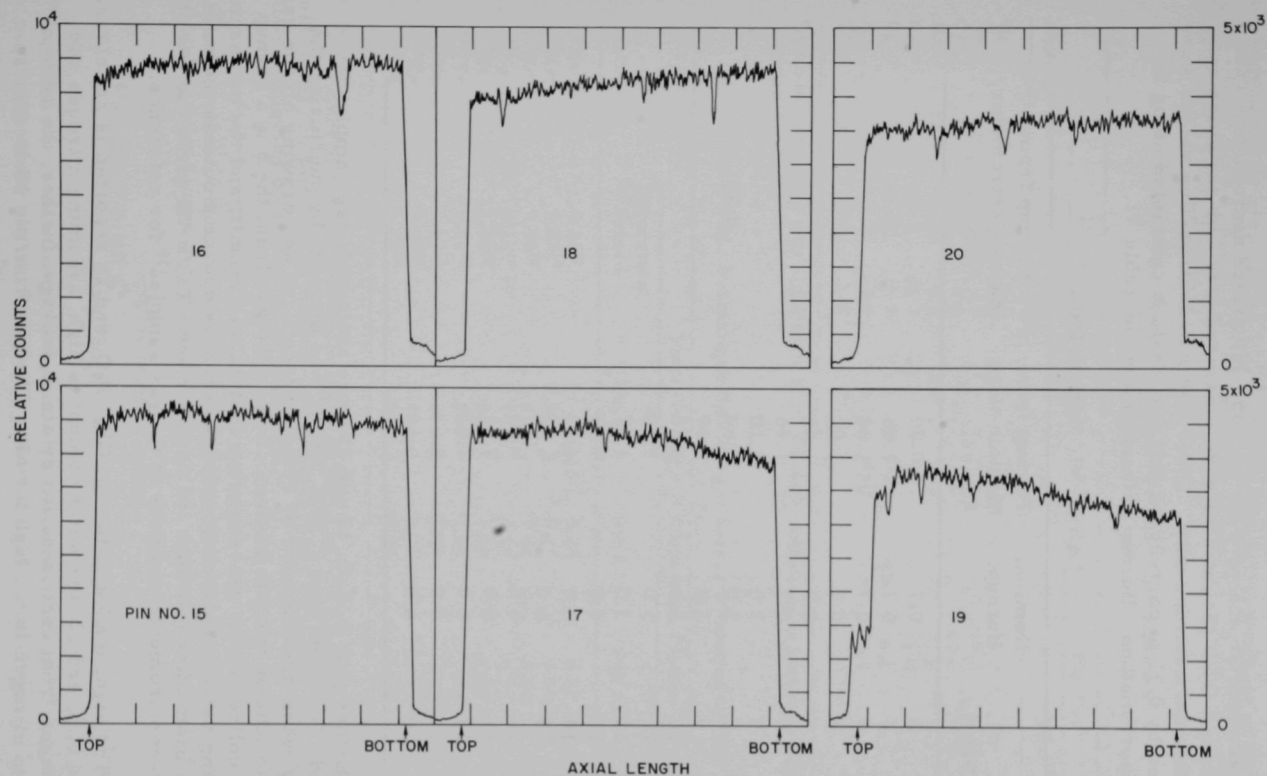
Fig. 5. Axial Gamma-ray Scan Data for Pins 15-20

112-8494

17

mass-spectrometer analyzed for burnup. Integrated neutron-flux values were obtained from the monitor wire measurements[15] by assuming activation by thermal neutrons only. These thermal-neutron-flux values were multiplied by 0.91 to correct for flux depressions calculated using the $S_n$ transport method. Burnup data are shown in Table VI.

TABLE VI. Burnup Data

| Pin No. | Nominal Burnup, a/o | Burnup from Monitor-wire Analysis, a/o | Burnup from Mass-spectrometer Analysis, a/o |
|---|---|---|---|
| 1 | 0.7 | 0.80 | - |
| 2 | 0.7 | 1.08 | 0.76 |
| 3 | 0.7 | 1.04 | - |
| 4 | 0.7 | 1.02 | - |
| 5 | 0.7 | 1.42 | - |
| 6 | 0.7 | 1.46 | 1.03 |
| 7 | 3.0 | 4.10 | - |
| 8 | 3.0 | 4.60 | 4.39 |
| 9 | 3.0 | 3.89 | - |
| 10 | 3.0 | 3.80 | - |
| 11 | 3.0 | 3.30 | - |
| 12 | 3.0 | 3.77 | 3.53 |
| 13 | 3.0 | 4.13 | - |
| 14 | 3.0 | 4.33 | - |
| 15 | 6.0 | 6.64 | - |
| 16 | 6.0 | 6.23 | - |
| 17 | 6.0 | 7.41 | - |
| 18 | 6.0 | 7.63 | - |
| 19 | 6.0 | 5.64 | - |
| 20 | 6.0 | 5.66 | - |

Before pins 2, 6, 8, 12 and 15 were sectioned, gas samples were collected. Gas from pins 2, 6, 8, and 12 was obtained by puncturing the cladding tubes mechanically by remote procedures and drawing off the gas into an evacuated vacuum system. Before the gas from the 6 a/o burnup pin was collected, the gas-sampling system was rebuilt, and the mechanical puncturing device replaced by a laser, which is operated outside the cave with the beam aimed through the cave window. Table VII gives the results of mass-spectrometer analyses of the gas samples[16] for reference.

The significance of the $H_2$, $CH_4$, $H_2O$, and $O_2$ reported is not clear. For pins 6, 8, and 12, the water content is high, assuming nitrogen and oxygen come from contamination by air in-leakage; further, the ratio of oxygen to nitrogen is too high for air. The gas from pin 15 is clearly

contaminated by air. Table VIII lists the measured amounts of fission gases from pins 6, 8, 12, and 15, normalized to $^{86}$Kr (which is formed as a primary fission product).*

TABLE VII. Results of Mass-spectrometer Analyses of Gas from Pins (in %)

| Gas | Pin No.[a] | | | | Gas | Pin No.[a] | | | |
|-----|------|------|------|------|-----|------|------|------|------|
|     | 6 | 8 | 12 | 15 |     | 6 | 8 | 12 | 15 |
| $H_2$ | 0.1 | 0.1 | 0.2 | 0.2 | $^{132}$Xe | 7.5 | 11.5 | 9.6 | 1.80 |
| He | - | 1.3 | 0.9 | <0.02 | $^{134}$Xe | 12.3 | 19.6 | 16.4 | 2.62 |
| $CH_4$ | 0.1 | <0.1 | 0.1 | <0.02 | $^{136}$Xe | 18.2 | 29.2 | 24.3 | 5.04 |
| $H_2O$ | 11.3 | 6.6 | 8.2 | 0.6 | $^{83}$Kr | 1.0 | 1.2 | 1.1 | 0.41 |
| $N_2$ | 18.6 | 8.4 | 15.7 | 68.1 | $^{84}$Kr | 1.7 | 2.8 | 2.4 | 0.57 |
| $O_2$ | 9.5 | 3.5 | 5.7 | 17.8 | $^{85}$Kr | 0.5 | 0.6 | 0.5 | 0.07 |
| Ar | 11.7 | 2.7 | 4.8 | 1.0 | $^{86}$Kr | 3.3 | 5.8 | 4.4 | 0.84 |
| $^{131}$Xe | 4.4 | 6.7 | 5.8 | 0.93 |     |   |   |   |   |

[a]Sample from pin 2 was apparently lost; the bulb containing it was reported to contain only air.

TABLE VIII. Normalized Fission-gas Release, Relative to $^{86}$Kr

| Isotope | Total Normalized Yield from Fission | | | | |
|---------|-------------|-------|-------|--------|--------|
|         | Theoretical Values | Pin 6 | Pin 8 | Pin 12 | Pin 15 |
| $^4$He | 0.15[17] | 0 | 0.22 | 0.21 | 0 |
| $^{83}$Kr | 0.27[18] | 0.30 | 0.21 | 0.25 | 0.49 |
| $^{84}$Kr | 0.50[18] | 0.51 | 0.48 | 0.54 | 0.68 |
| $^{85}$Kr | 0.15[18] | 0.14 | 0.11 | 0.12 | 0.08 |
| $^{86}$Kr | 1.00[18] | 1.00 | 1.00 | 1.00 | 1.00 |
| $^{131}$Xe | 1.45[18] | 1.33 | 1.15 | 1.32 | 1.11 |
| $^{132}$Xe | 2.17[18] | 2.29 | 1.96 | 2.20 | 2.14 |
| $^{134}$Xe | 3.99[18] | 3.74 | 3.35 | 3.75 | 3.12 |
| $^{136}$Xe | 3.19[18] | 5.54 | 4.99 | 5.56 | 6.00 |

Except for the anomalously high yield of $^{136}$Xe and low yield of $^{85}$Kr, especially in pin 15, the fission-gas compositions reported are close to those expected on the basis of total fission yield.**

---

*A small amount of $^{86}$Kr is obtained not as a primary fission product, but as a daughter element from the following fission-fragment decay chain:

$$^{87}Se(17S) \rightarrow {}^{87}Br(55S) \Big\langle {}^{\sim 2\% \ ^{86}Kr(Stable) \ + \ neutron}_{\sim 98\% \ ^{87}Kr(78 \ m) \ \rightarrow \ ^{87}Rb(6 \ \times \ 10^{10} \ yr).}$$
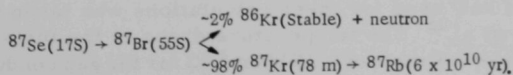
**Corrections due to neutron absorption in the relatively high-cross-section isotopes $^{131}$Xe and $^{83}$Kr would change these ratios by less than 1% (less than the estimated uncertainties in the data).

Table IX lists the measured gas yields from pins 2, 6, 8, 12, and 15, along with the total amount expected for 100% gas release from the oxide.[17,18] Volumes are referred to 760 mm Hg and 22°C. Table IX is valid only if the air in-leakage occurred after the gas-volume measurement.

TABLE IX. Measured Gas Yields for Pins 2, 6, 8, 12, and 15

| Pin No. | Burnup, a/o | Measured Gas Volume, cc | Gas Volume for 100% Release, cc | Release, % |
|---------|-------------|-------------------------|----------------------------------|------------|
| 2 | 1.08 | 1.2 | 3.7 | 32 |
| 6 | 1.46 | 1.4 | 4.9 | 29 |
| 8 | 4.60 | 3.7 | 15.8 | 23 |
| 12 | 3.77 | 3.7 | 13.0 | 28 |
| 15 | 6.64 | 5.3 | 22.8 | 23 |

The release values of Table IX may be compared with releases of 42, 25, and 18% estimated for 0.7, 3, and 6 a/o burnup, respectively.[19] The estimates are based on calculations of steady-state fuel-pin temperature distributions after the change in fuel geometry from a solid cylinder to an annulus, and on a generalized release correlation for $UO_2$ steady-state irradiations[20] given by Lewis.* The calculated release values decrease with burnup, because the $^{235}U$ depletion during steady-state irradiation produced large decreases in fuel temperature during irradiation. The changes in fuel temperatures calculated are shown in Fig. 6, which has the initial radial temperatures for the solid cylinder** and four curves for an annulus with inner diameter of 0.116 cm: one curve for no $^{235}U$ depletion,** one for 4% depletion corresponding to power at 0.5 a/o burnup,† one for 15% depletion corresponding to power at 1.9 a/o burnup,† and one for 25% depletion corresponding to power at 4 a/o burnup.† The integral of kdT used for these calculations was taken from a review paper by Pashos et al.[22] The temperature drops in the fuel-cladding gap were calculated using an estimate of 0.25 $W/cm^2$ °C for the gap conductance.**
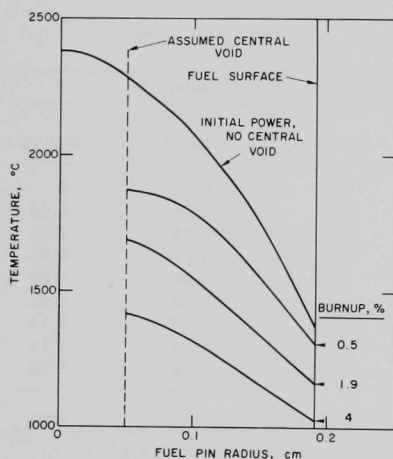


113-1519

Fig. 6. Calculated Radial Temperature Distributions of Fuel during Steady-state Irradiation

---

*See the discussion of Fig. A-1 in Ref. 20.

**Calculated with U = 0.2 $J/cm^2$-°C, the design value, which was reported for similar unirradiated pins.[21]

†Calculated with U = 0.25 $J/cm^2$-°C as typical of the irradiated pins. (See Section III.C in Ref. 6.)

Because of the large uncertainties in this conductance, and because of possible variations in conductance along the pin, as well as power-distribution changes in MTR during irradiation, the Fig. 6 curves should be considered to be reference temperatures only.

Neutron radiography was used to check the macroscopic internal condition of all pins. Axial segmentation of the fuel was shown clearly. Careful examination of the original prints disclosed that the irradiation had formed central voids, of the order of 0.1-cm diameter. Figure 7 is a composite reproduction of the neutron radiographs of even-numbered pins 2-14. In addition to the gaps and central voids, the figure also shows bottom end fittings, top end fittings and axial restrainers,* and spiral spacer wires. The conditions recorded in Fig. 7 are typical of those found for odd-numbered pins 1-13. Figure 8 is a composite radiograph of all the highest-burnup pins (15-20). The appearance is similar to that of Fig. 7. As before, central voids were visible on the originals.

X-ray photographs were taken of the pins to supplement the neutron radiography. Although the X rays gave poorer penetration of the fuel, they gave photographs showing fuel edges, cladding, and the degree of fine fuel fragmentation much more clearly than in Figs. 7 and 8. Figure 9 is a composite of the X-ray photographs for pin 6. Some oxide fragmentation has occurred but there is no significant powdering of the ceramic fuel. Note that, as a result of handling, the top fuel piece has shifted closer to the restrainer than shown for pin 6 in Fig. 7.

*Axial restrainers were not in contact with the fuel; they were used only to prevent gross displacement of oxide during handling and shipping. (See Fig. 7.)

22
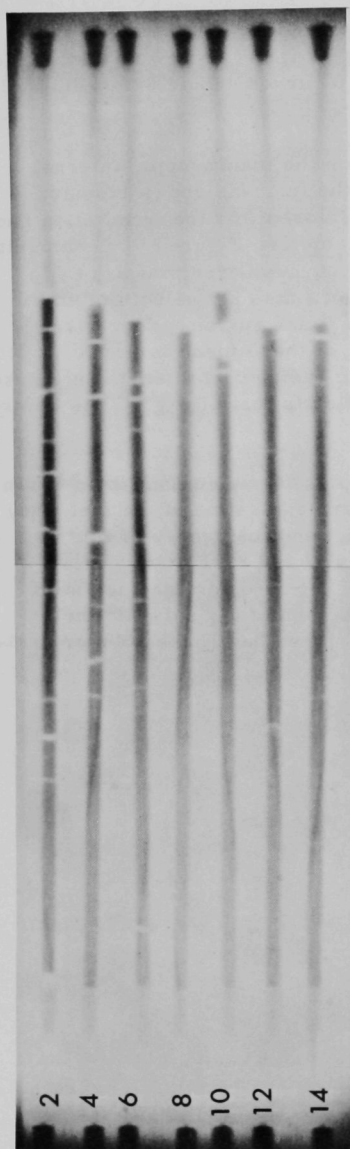


112-6755

Fig. 7. Composite Neutron Radiograph
of Even-numbered Pins 2-14

112-8497

Fig. 8. Composite Neutron Radiograph
of High-burnup Pins 15-20

112-6805

Fig. 9. Postirradiation
X-ray Photo-
graph of Pin 6

## C. Ceramographic Examinations

Microstructures of the five control specimens--pins 2 and 6 (0.7 a/o burnup group), pins 8 and 12 (3 a/o burnup group), and pin 15 (6 a/o burnup group)--were examined at three locations along the axis. The general appearance of the microstructure is typical of that of irradiated, sintered, high-density $UO_2$ fuel.[23] Representative photomicrographs and measurements are shown in Figs. 10-16. In each of the figures, a typical X-ray photograph (of pin 6) is included to provide a consistent basis for indicating the regions from which specimens were taken for examination.

The specimens were vacuum-impregnated with room-temperature-setting epoxy resin at the time of mounting. Several specimens required reimpregnation before the 600-grit stage of grinding to prevent sample loss. A 10% solution of sulphuric acid in 30% hydrogen peroxide was used as an etchant.

The diameter of the fuel was obtained by subtracting the known cladding thickness, plus the thickness of annulus between fuel and cladding as measured on the micrograph, from the outside diameter of the pin as measured with a micrometer after irradiation.

Detailed discussion of the five pins given destructive examinations follows.

### 1. Pin 2

A longitudinal section taken from pin 2 at the location shown in Fig. 10a is shown (unetched) as Fig. 10b. Note the bright inclusion of metallic appearance.* Figure 10c is a closeup of the inclusion. Figures 10d and e show similar material at higher magnifications. In general, the appearance of pin 2 was similar to that of pin 6 (below).

### 2. Pin 6

A cross section was taken from the top of pin 6, as shown in Fig. 11a. This cross section (etched) is Fig. 11b. The fuel, originally of 0.381-cm diam, has become oval with a major axis of 0.384 cm and a minor diameter of 0.381 cm (representing an average diametral growth of 0.3%). The central void is oval: the major axis is 0.043 cm, and the minor axis is 0.033 cm. The central-void cross-sectional area is 1% of that of the fuel. Figure 11c is a closeup of the fuel, showing the postirradiation pore distribution. Figures 11d and e show higher magnifications, giving enlarged views of the fuel structure.

---

*See Section D.2 below for electron-microprobe identification of the inclusion.
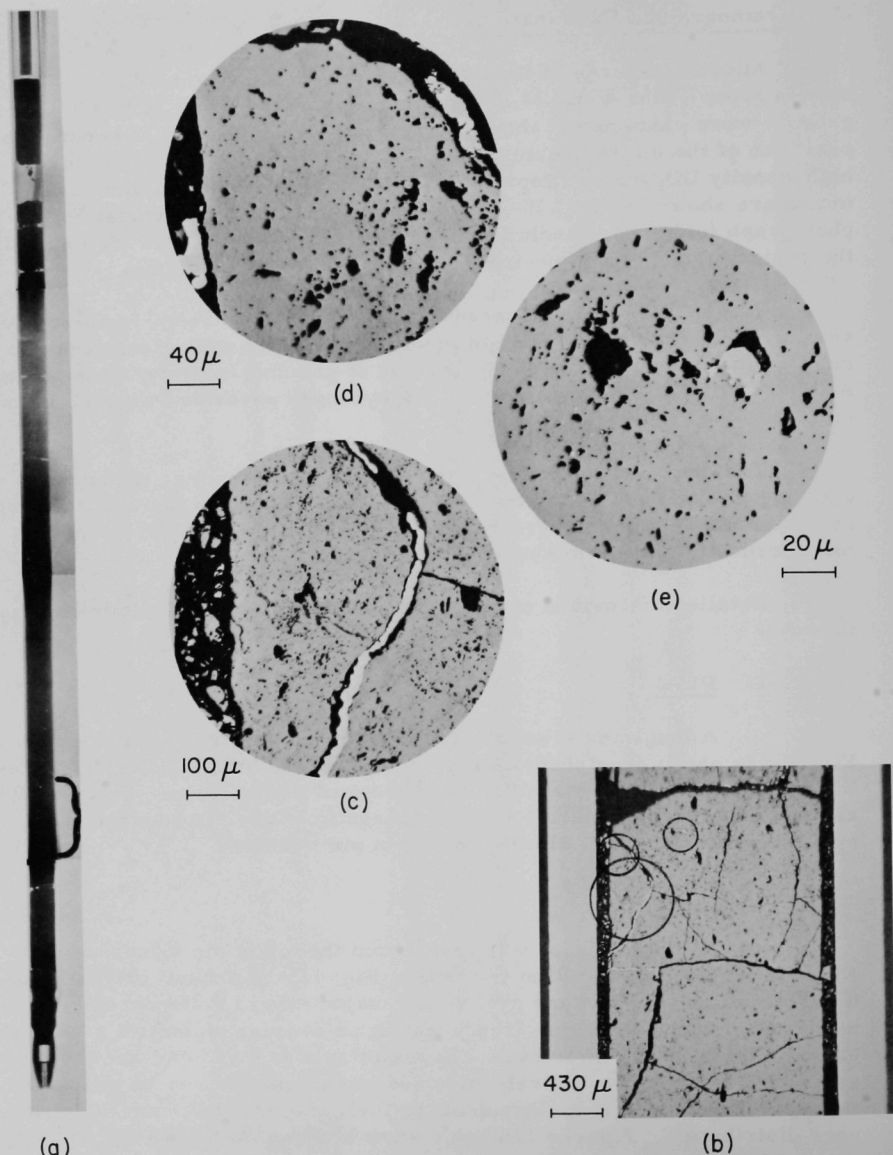
112-7440

Fig. 10. Microscopic Views of Longitudinal Section of Pin 2. (a) Typical X-ray photo (of pin 6) showing location of specimen; (b) Longitudinal section of specimen showing white inclusions in cracks and pores and between fuel and cladding; (c) Enlargement showing white inclusion in crack; (d) Higher enlargement of typical white inclusion; and (e) Enlarged detail of speck in pore.

40 μ

(e)

40 μ

(d)

430 μ

100 μ

(a)                    (b)                    (c)
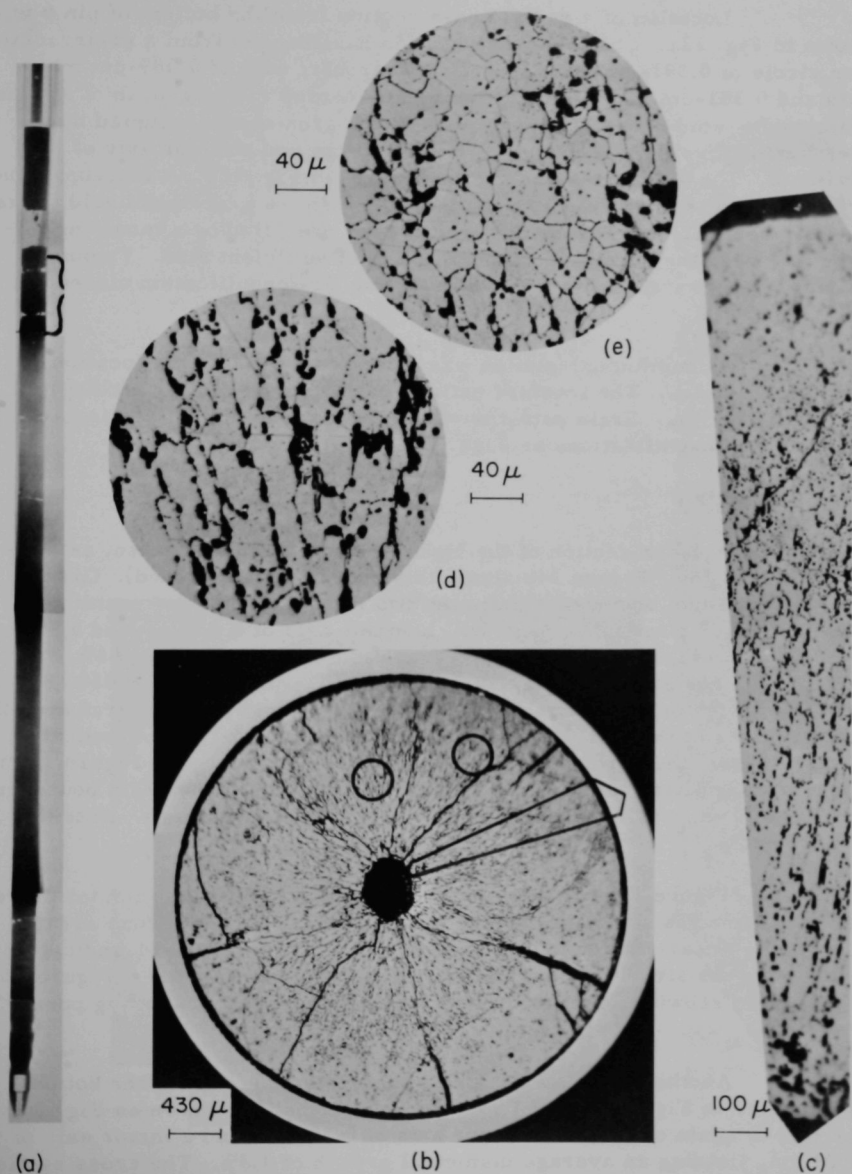
112-7442

Fig. 11. Microscopic Views of Radial Cross Section of Pin 6 near Top of Pin. (a) X-ray photo showing location of specimen; (b) Radial cross section of specimen; (c) Enlargement of area indicated on specimen; (d) Enlargement showing columnar grains near central void; and (e) Enlargement showing small grains near periphery.

Location of a radial cross section from the bottom of pin 6 is shown in Fig. 12a. The fuel cross section has changed from a preirradiation circle of 0.381-cm diam to a nearly circular oval of 0.389-cm major axis and 0.381-cm minor axis, yielding an average radial growth of approximately 1%. Void cross section is 4.3% of the area shown occupied by the fuel; the oval void has a major axis of 0.086 cm and a minor axis of 0.074 cm. These features are shown (etched) in Fig. 12b. A closeup of the cross section is presented as Fig. 12c, which shows cracks and void areas at grain boundaries. These voids and cracks are filled by a mounting impregnant when they are interconnecting and of sufficient size. Typical columnar grain structure is shown in the higher-magnification closeup of Fig. 12d.

A longitudinal section was taken from pin 6 at the location shown in Fig. 13a. The fracture pattern in this section (after etching) is shown in Fig. 13b. Grain patterns visible in the longitudinal section are given in two magnifications as Figs. 13c and d.

3.  Pin 8

A cross section of the higher-burnup pin 8 was taken, as indicated in Fig. 14a. Figure 14b shows this cross section (etched). Greater growth of the fuel occurred than in the two lower-burnup pins examined. The postirradiation fuel is oval, with a major axis of 0.389 cm and a minor axis of 0.386 cm, representing an average diametral growth of 1.6%. The central void has a major axis of 0.099 cm and a minor axis of 0.058 cm. Note the profusion of nearly circular dark spots of porous appearance in the outer regions of the fuel. Figure 14c is a closeup of the region indicated; in some cases, the porous areas are traversed by fractures. Figure 14d is a higher-magnification closeup showing porous areas. The grain boundaries appear to have been destroyed in well-developed porous areas. Note the bright specks.

Figure 15 shows the location of a longitudinal section taken from pin 8. Figure 15b shows this cross section (etched). The porous areas appear to be nearly circular in this view, as well as in Fig. 14, indicating that the porous structures are spherical, rather than fiberlike. Figure 15c is a closeup showing some grain boundaries in a region containing porous areas.

Another cross section from pin 8 was taken from the bottom, as indicated in Fig. 16a. The cross section (etched) is shown as Fig. 16b. The fuel is again oval, with a major axis of 0.389 cm and a minor axis of 0.384 cm, yielding an average diametral growth of 1.3%. The cross section of the central void has a major axis of 0.081 cm and a minor axis of 0.056 cm. The cross-sectional area of the void is 3.2% that of the postirradiation area of the fuel. Figures 16c and d are higher-magnification photomicrographs of the fuel from this section.

Fig. 12. Microscopic Views of Radial Cross Section of Pin 6 near Bottom of Pin. (a) X-ray photo showing location of specimen; (b) Radial cross section of specimen; (c) Enlargement of area indicated on specimen; and (d) Enlargement showing columnar grains near center.
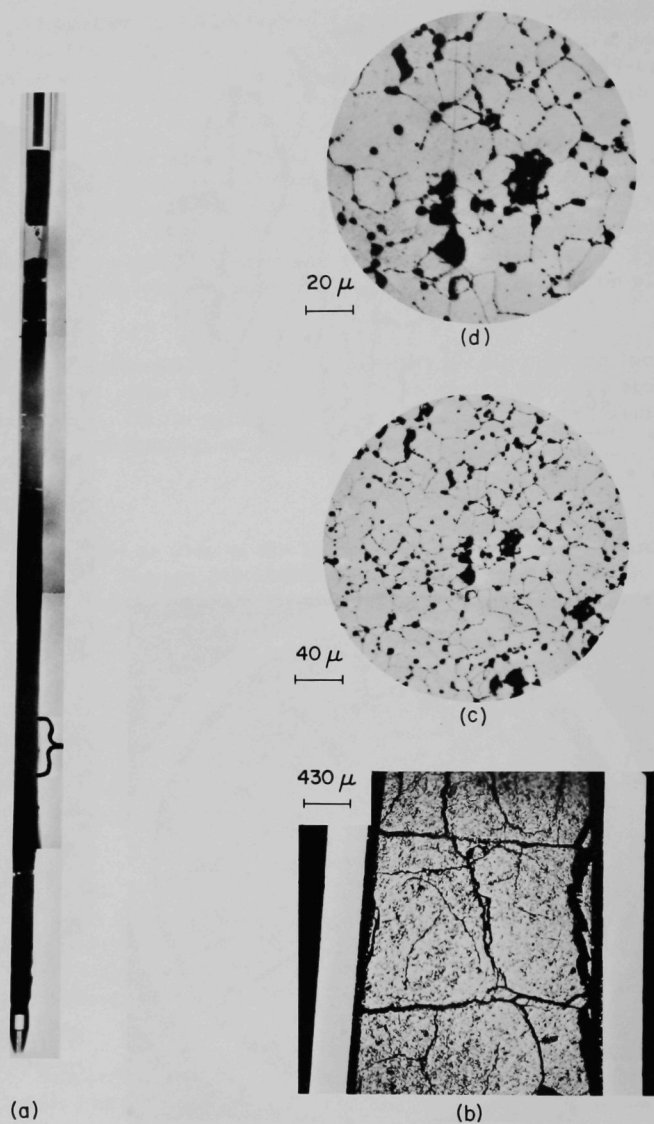
112-7436

Fig. 13. Microscopic Views of Longitudinal Section of Pin 6. (a) X-ray photo
showing location of specimen; (b) Longitudinal section of specimen;
(c) Enlargement of area indicated on specimen; and (d) Detail of
enlargement.

(a)

112-7445

(d)

(b)

(c)
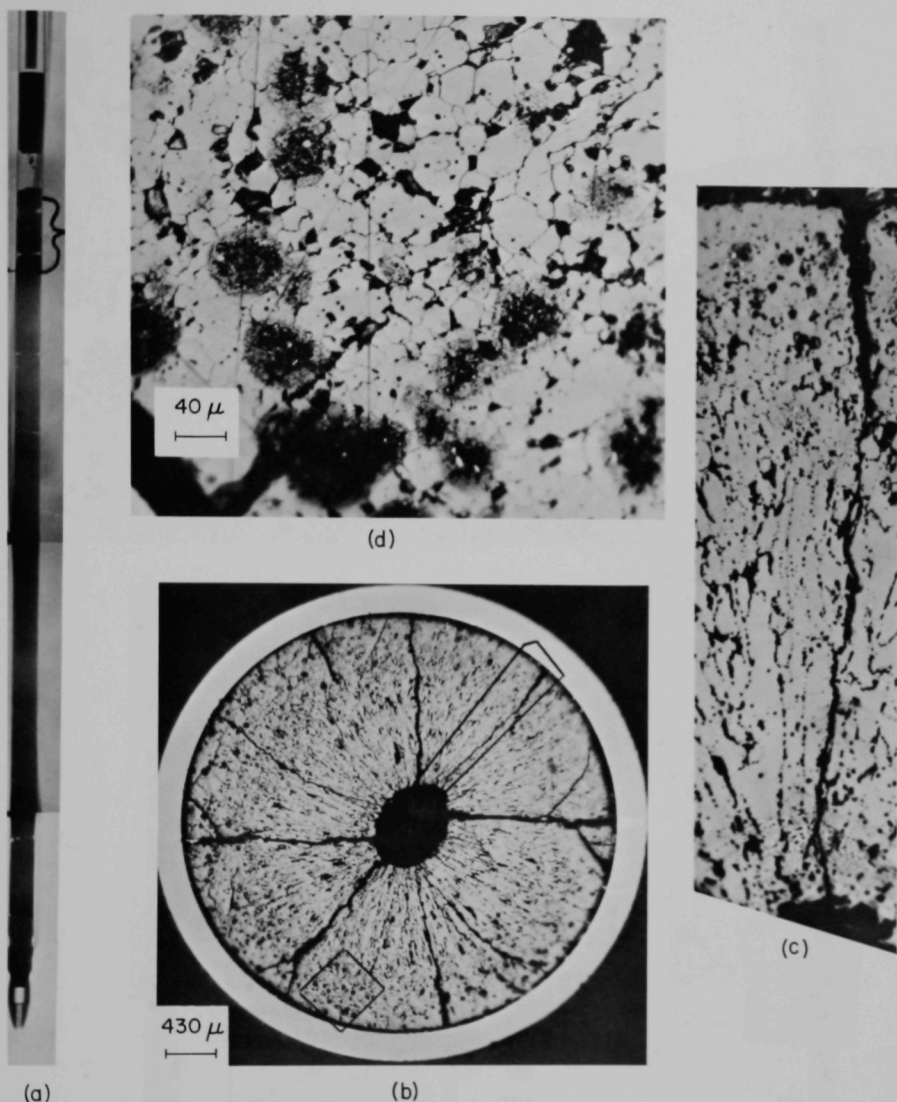
Fig. 14. Microscopic Views of Radial Cross Section of Pin 8 near Top of Pin. (a) Typical X-ray photo (of pin 6) showing location of specimen; (b) Radial cross section of specimen; (c) Enlargement of area indicated on section; (d) Higher enlargement of area showing small grains and porous regions with white inclusions.
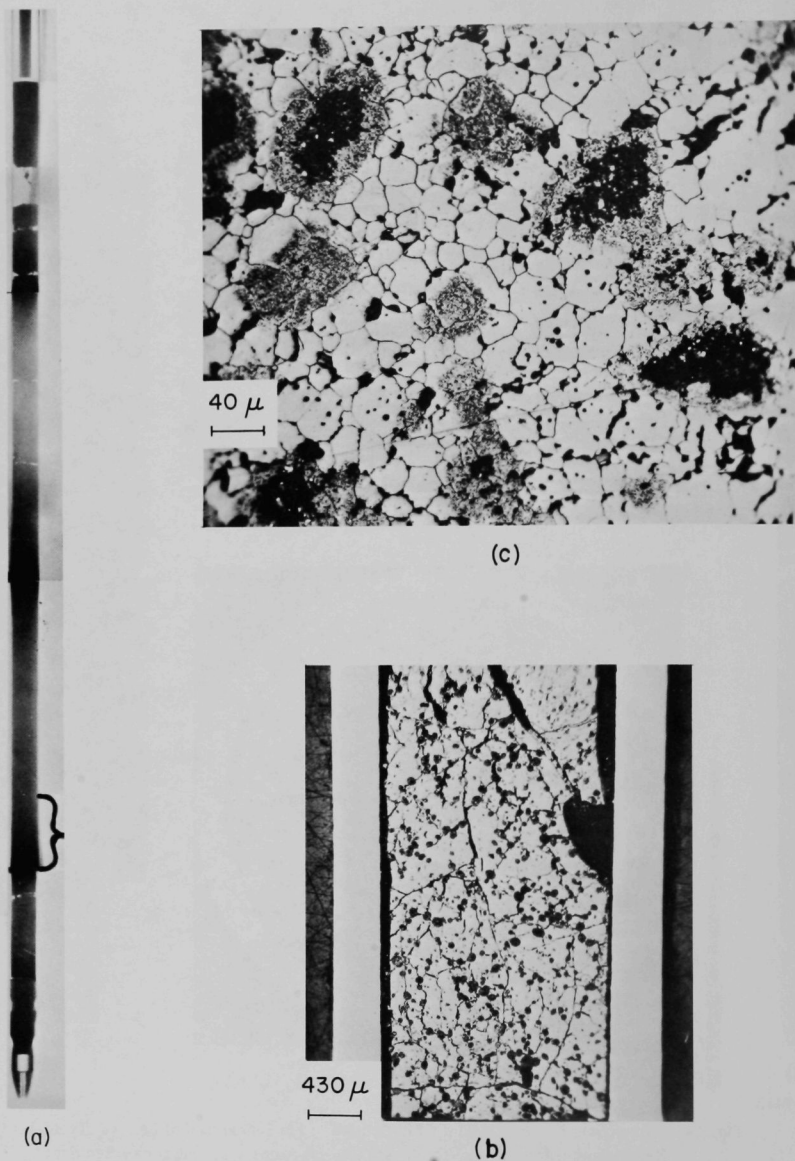
112-7441

Fig. 15. Microscopic Views of Longitudinal Section of Pin 8. (a) Typical X-ray photo (of pin 6) showing location of specimen; (b) Longitudinal section of specimen showing porous regions; and (c) Enlargement of section showing small grains near periphery, and some porous regions.

40 μ

(d)

430 μ

(b)

100 μ

(c)

(a)

112-7446

Fig. 16. Microscopic Views of Radial Cross Section of Pin 8 near Bottom of Pin. (a) Typical X-ray photo (of pin 8) showing location of specimens; (b) Radial cross section of specimen; (c) Enlargement showing area from central void to periphery, and (d) Higher enlargement showing porous region with white inclusions.

4. <u>Pin 12</u>

The condition of pin 12 was similar to that of pin 8 and will not be reviewed in detail here. Figure 17 compares a ceramographic section from pin 12 with a direct-contact autoradiograph enlarged to the same size as the photographic view. Centers of activity, or "hot spots," appear as white areas on the autoradiograph. Direct comparison of the photograph (Fig. 17a) with the autoradiograph (Fig. 17b) shows that the porous areas alone produce the hot spots near the periphery. Nearer the center of the fuel, the centers of activity become diffuse. Cladding is not visible in the autoradiograph because of the relatively low activity of the cladding.

The "hot spots" (or porous areas) are probably caused by particles of fully enriched $UO_2$, which become regions of very high burnup under irradiation. The size of the porous areas is approximately the same as the size of the enriched oxide particles which were blended with natural-enrichment oxide powder to obtain the specified 13% enrichment of the fuel bodies. Lack of hot spots or porous areas in the high-temperature central region may be due to diffusion of fission products and enriched oxide during "in-pile sintering." (Figure 1 shows the preirradiation distribution of uranium.)

5. <u>Pin 15</u>

Figure 18 is a diagrammatic reproduction of the high-burnup pin 15 showing the pin with its end fittings and, within, the five stacked oxide pellets. The figure indicates specific locations of the oxide interfaces with reference to the base line at the bottom of the fuel column. To the left of the diagram is shown an X-ray photograph of pin 15, which corresponds to the diagram. The labeled segments of the diagram (A, B, C, D) identify samples from three regions of pin 15 (top, central, and bottom), listing the specific analysis performed on each sample.

6. <u>A Samples</u>

Samples $A_1$, $A_2$, and $A_3$ from the bottom, center, and top, respectively, of pin 15 were chosen exclusively for burnup determination by mass-spectrochemical and radiochemical analysis because of their specific location along the axis of the pin. The underlying reason for this was to determine the extent that fission-product migration occurs along the axis of the pin from the center to the ends.

7. <u>B Samples</u>

Samples $B_1$, $B_2$, and $B_3$ representing the bottom, central, and top regions, respectively, of pin 15 were prepared for analysis of the composition by an electron-microprobe analyzer. (See Section II.D.)

430 μ

(b)



430 μ
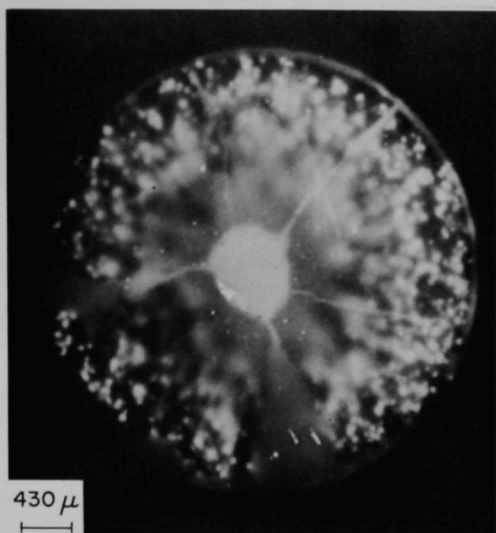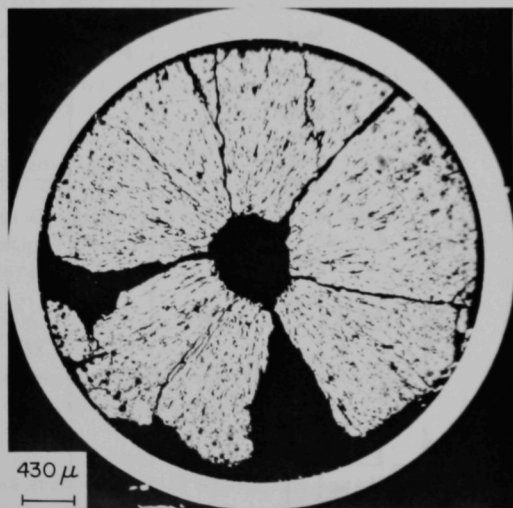
(a)

112-7435

Fig. 17.  Microscopic Views of Radial Cross Section of Pin 12.
(a) Photograph of radial cross section; and (b) Auto-
radiograph of cross section.

34
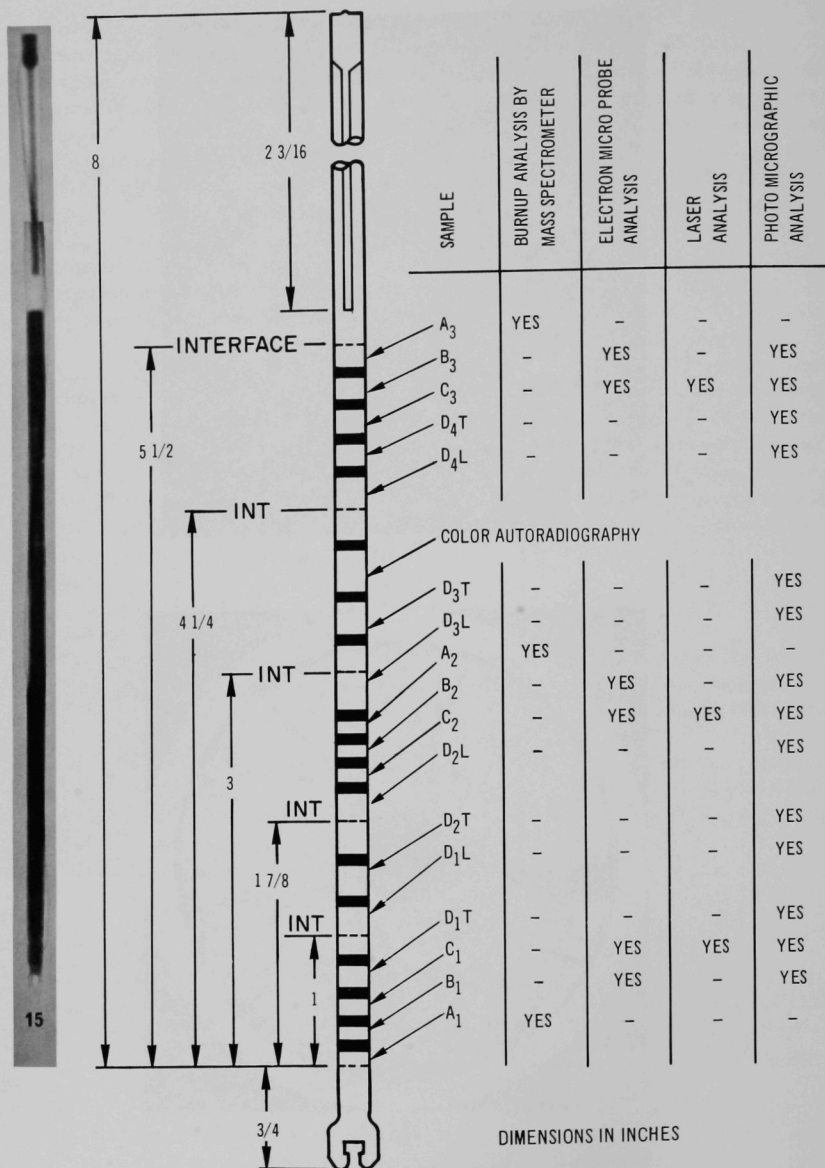


112-8892

Fig. 18. X-ray Photograph of Pin 15 Showing Sample Locations and Types of Analyses Performed

Figure 19a is a photomicrograph of sample $B_1$ showing its full cross section, which was exposed to the electron-microprobe analyzer. Figures 19b and c (respectively) are beta-gamma and alpha autoradiographs of sample $B_1$ at the same magnification as that of Fig. 19a. These auto-radiographs show clearly that the porosity spots alone are the source for beta-gamma and alpha radiation, and that this radiation, representing the uranium constituent of the $UO_2$ matrix, is nonhomogeneously distributed throughout.

Only half of the full cross section of sample $B_2$ remained after grinding and polishing. The results of the electron-microprobe analysis showed that there is no significant difference in analysis among the B samples.

Figure 20a is a photomicrograph of the cross section of sample $B_3$. Alpha and beta-gamma autoradiographs appear as Figs. 20b and c, respectively. These show that the porous areas alone produce the "hot spots" near the periphery. Near the center of the fuel, the activity becomes diffused.

In all the samples examined, numerous small inclusions varying from 1 to 15 $\mu$ in diameter and having a metallic luster were dispersed throughout the $UO_2$ matrix. In addition, large, round, porous inclusions up to 100 $\mu$ in diameter (these show up as dark spots in the photomicrographs) were dispersed through the outer one-fourth of the radius of the fuel. The analysis of these porous areas using an electron-microprobe analyzer is given in Section II.D.

8.  C Samples

The C samples were specifically prepared for determining the relative amounts of fission products by the laser vaporization technique, which uses a laser beam to vaporize highly-localized parts of the sample.

9.  $D_T$ Samples

The eight D samples were divided into two categories, transverse and longitudinal, denoted by the subscript T and L, respectively.

The transverse D samples ($D_1T$, $D_2T$, $D_3T$, and $D_4T$) represent areas of interest directly adjacent to longitudinal samples from the bottom, center, and top of the pin and will be compared against one another here regarding their overall appearance, diametric change, diametric growth, center-core dimensions, annulus spacing, area ratio (void-to-expanded fuel), and grain growth.

(b)

475 μ

(c)

475 μ

(a)

475 μ
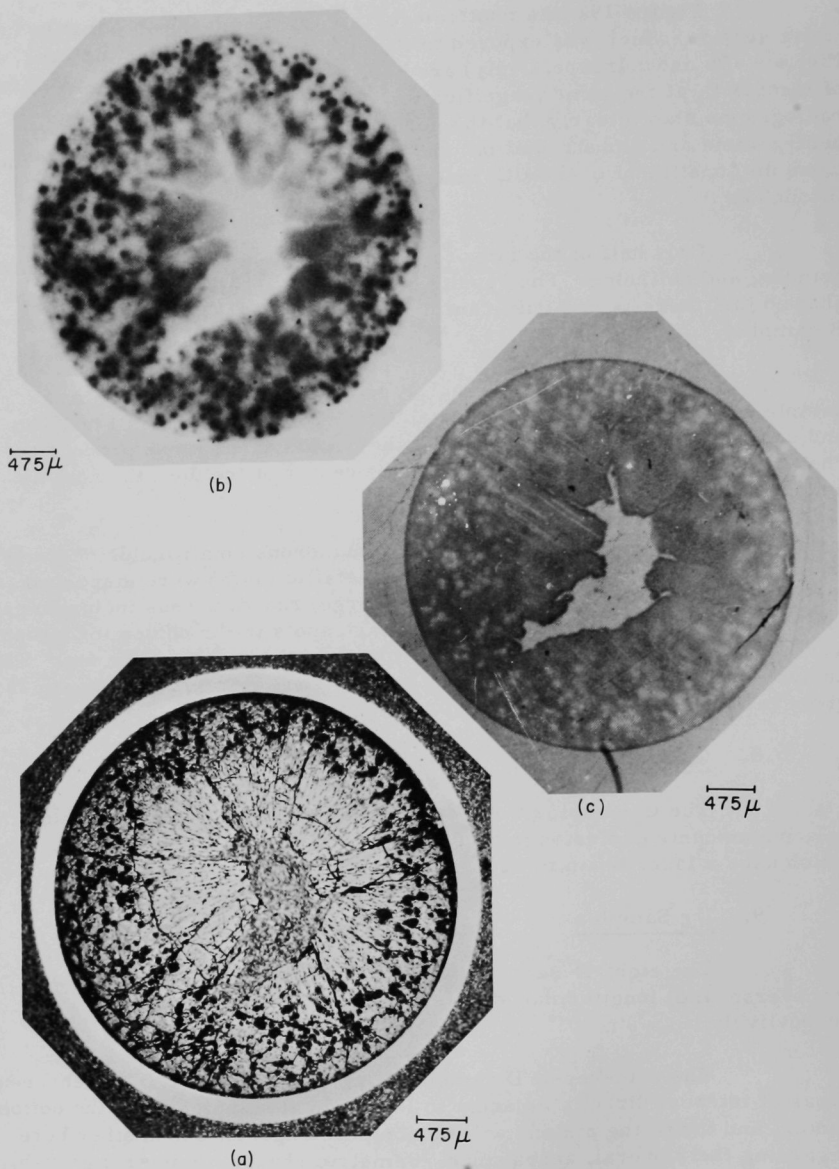
112-8897

Fig. 19. Microscopic Views of Radial Cross Section of Sample $B_1$ Taken from Pin 15. (a) Radial cross section; (b) Beta-gamma autoradiograph; and (c) Alpha autoradiograph.

(b)

475 μ

(c)

475 μ

(a)

475 μ
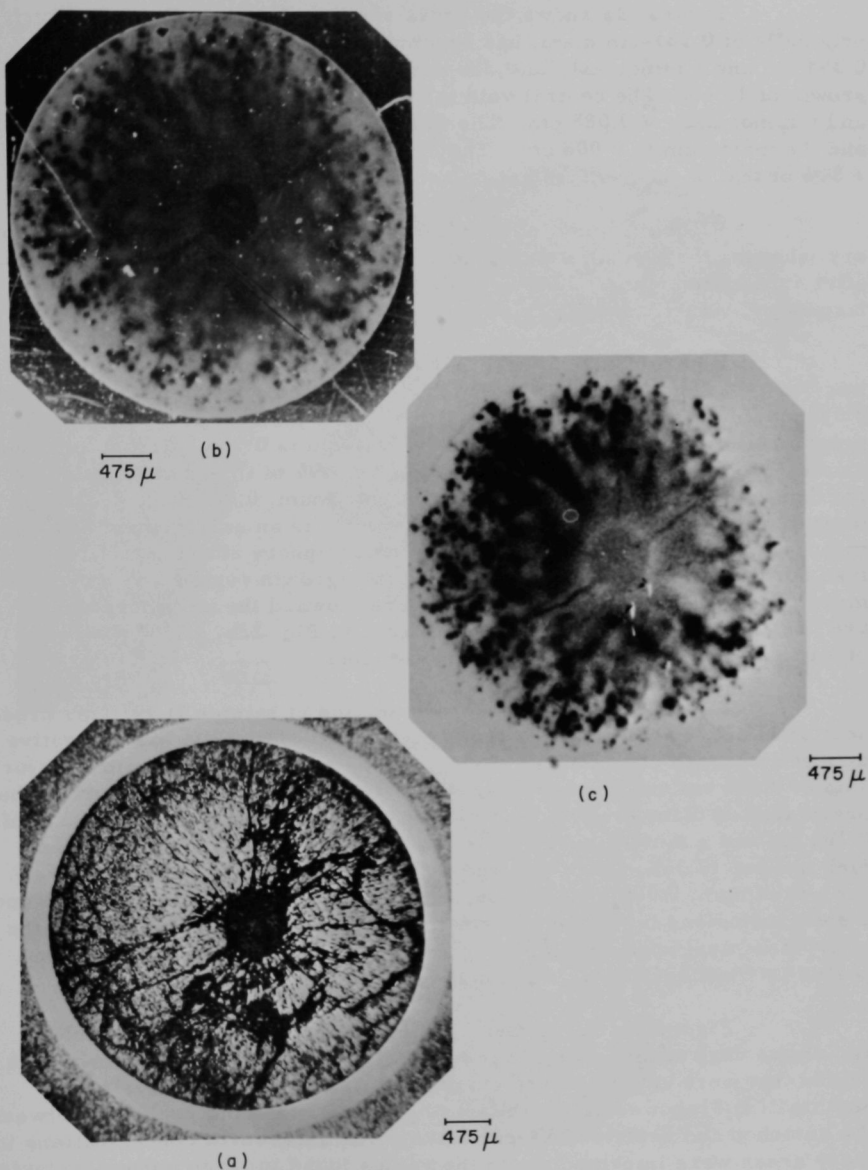
112-8898

Fig. 20. Microscopic Views of Radial Cross Section of Sample $B_3$ Taken from Pin 15. (a) Radial cross section; (b) Alpha autoradiograph; and (c) Beta-gamma autoradiograph.

Figure 21a shows the cross section of sample $D_1T$. The fuel, originally of 0.381-cm diam, has become oval with a major axis of 0.394 cm and a minor axis of 0.388 cm, representing an average diametric growth of 1.66%. The central void is oval, having a major axis of 0.042 cm and a minor axis of 0.085 cm. The minimum annulus spacing is 0.001 cm, and the maximum is 0.008 cm. The central void cross-sectional area is 1.84% of that of the postirradiation area of the fuel.

Figure 21b is a closeup of the fuel, from the core to the periphery, showing the typical distribution of pores and inclusions that appeared after irradiation. Figure 21c is a higher magnification showing the enlarged fuel structure and inclusions.

Figure 22a shows the full cross section of sample $D_2T$, which was changed from the preirradiation circle of 0.381-cm diam to an oval of 0.392-cm major axis and 0.381-cm minor axis, yielding an average radial growth of 1.4%. The major axis of the oval void is 0.060 cm, and the minor axis is 0.042 cm. The void cross section is 1.8% of the area occupied by the fuel. Annulus spacings were, for the minimum, 0.001 cm; for the maximum, 0.008 cm. Figure 22b (30-sec etch) is an enlargement of a segment of cross section from the core to the periphery showing the five diffuse porous areas within the columnar grain-growth region which become more concentrated and develop into spheres toward the periphery. Figure 22c is a further enlargement of an area in Fig. 22b, giving a closeup of a typical gray inclusion among porous spots.

Figure 23a shows the cross section of sample $D_3T$. This cross section is not typical of others that were examined since it has a negative diametric growth of -3.33%. The postirradiated fuel is oval, with a major axis of 0.356 cm and a minor axis of 0.307 cm, which are both short of the preirradiated diameter of 0.381 cm. The central void has a major axis of 0.162 cm and a minor axis of 0.116 cm. This yields a void-to-expanded-fuel ratio of 17.36%, which is highly unusual. The annulus spacings are, for a minimum, 0.008 cm, and for a maximum, 0.046 cm. Figures 23b and c show inclusions in the stainless steel cladding, which are similar to the microstructural appearance of $UO_2$ fuel dispersion in stainless steel reported by Cunningham, Beaver, and Waugh.[24]

Figure 24a is a cross-sectional view of sample $D_4T$ (etched) and shows dark areas interspersed throughout the columnar grain-growth region that were unseen before etching. The microprobe analysis (in Section III.D.3) showed these to be areas of partial isotopic exchange between the enriched and depleted $UO_2$ particles. The rare-earth concentrations in these areas were intermediate to the values found in large porous inclusions in the outer periphery and the major portion of the oxide matrix in the columnar grains.
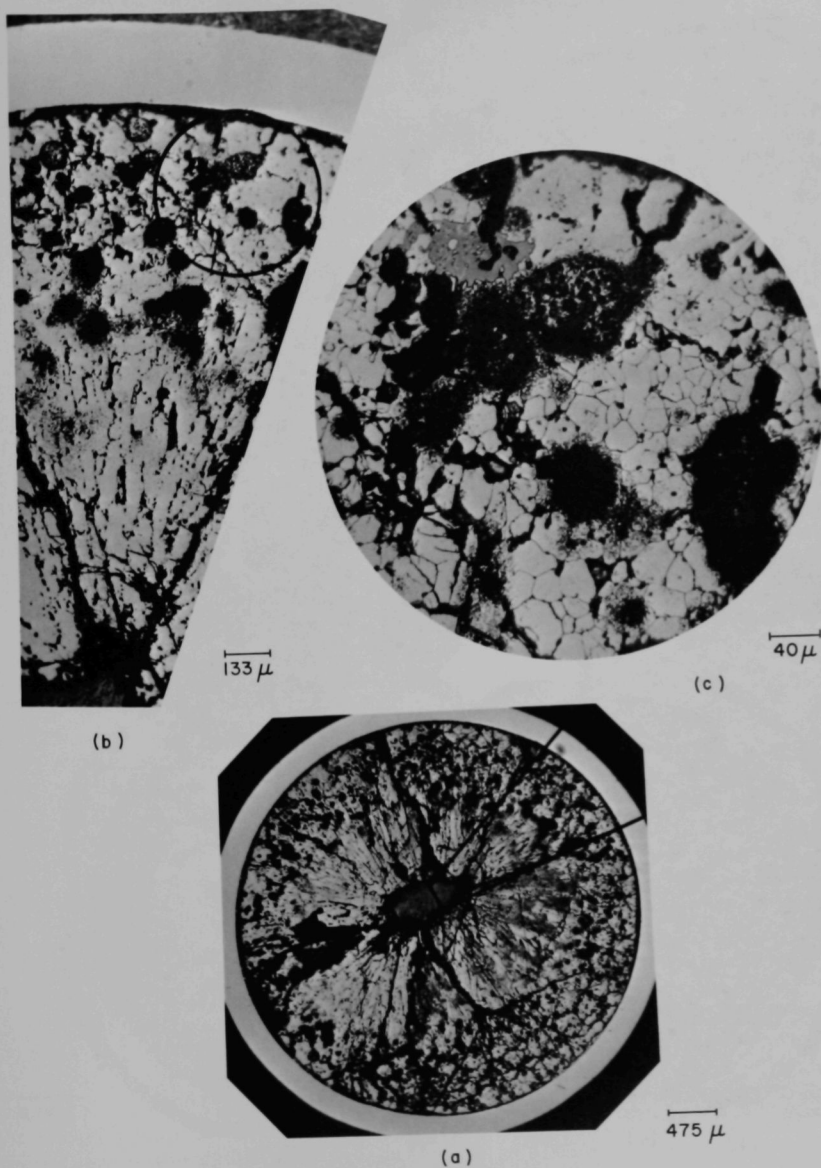
Fig. 21. Microscopic Views of Radial Cross Section of Sample $D_{1T}$ Taken from Pin 15. (a) Radial cross section; (b) Enlargement of area indicated on cross section; and (c) Higher enlargement of area indicated in (b).
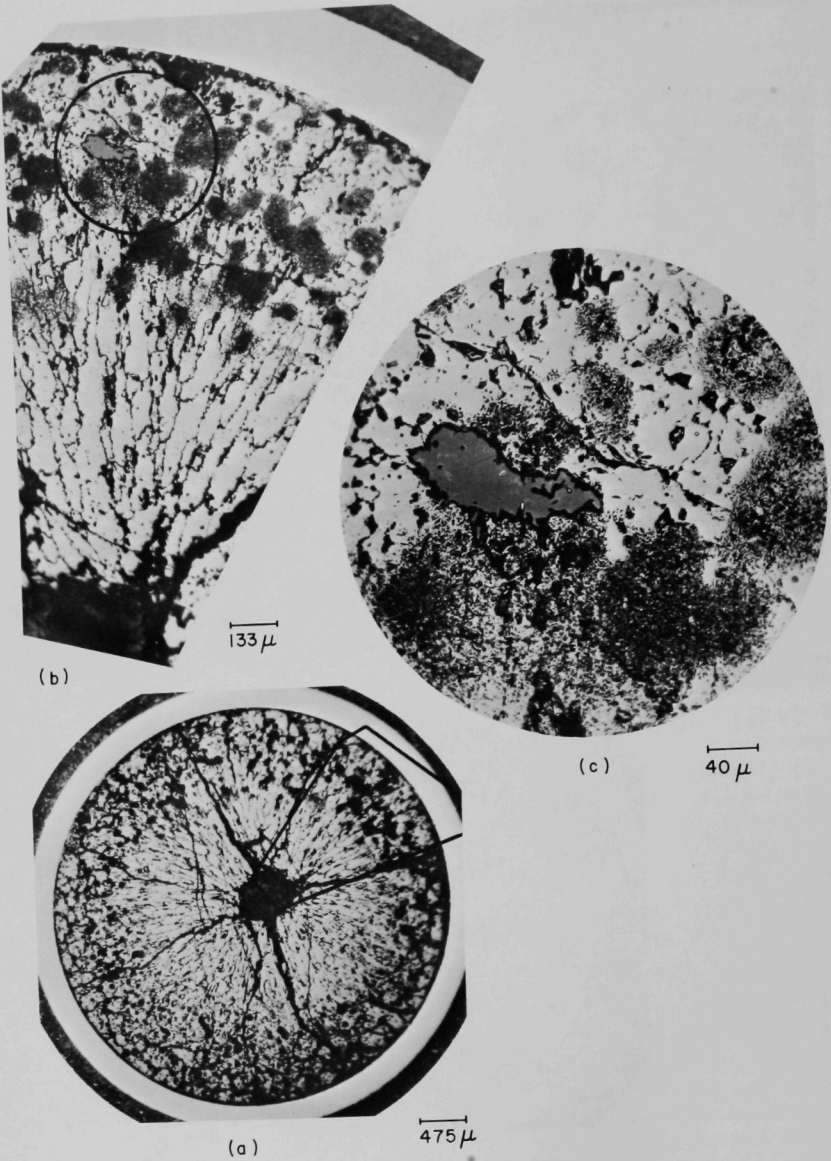
112-8896

Fig. 22. Microscopic Views of Radial Cross Section of Sample $D_2T$ Taken from Pin 15. (a) Radial cross section; (b) Enlargement of area indicated on cross section; and (c) Higher enlargement of area indicated in (b).

133 μ     (b)

475μ     (a)     40 μ     (c)

112-8899

Fig. 23. Microscopic Views of Radial Cross Section of Sample $D_{3T}$ Taken from Pin 15. (a) Radial cross section; (b) Enlargement of area indicated on cross section; and (c) Higher enlargement of cladding.
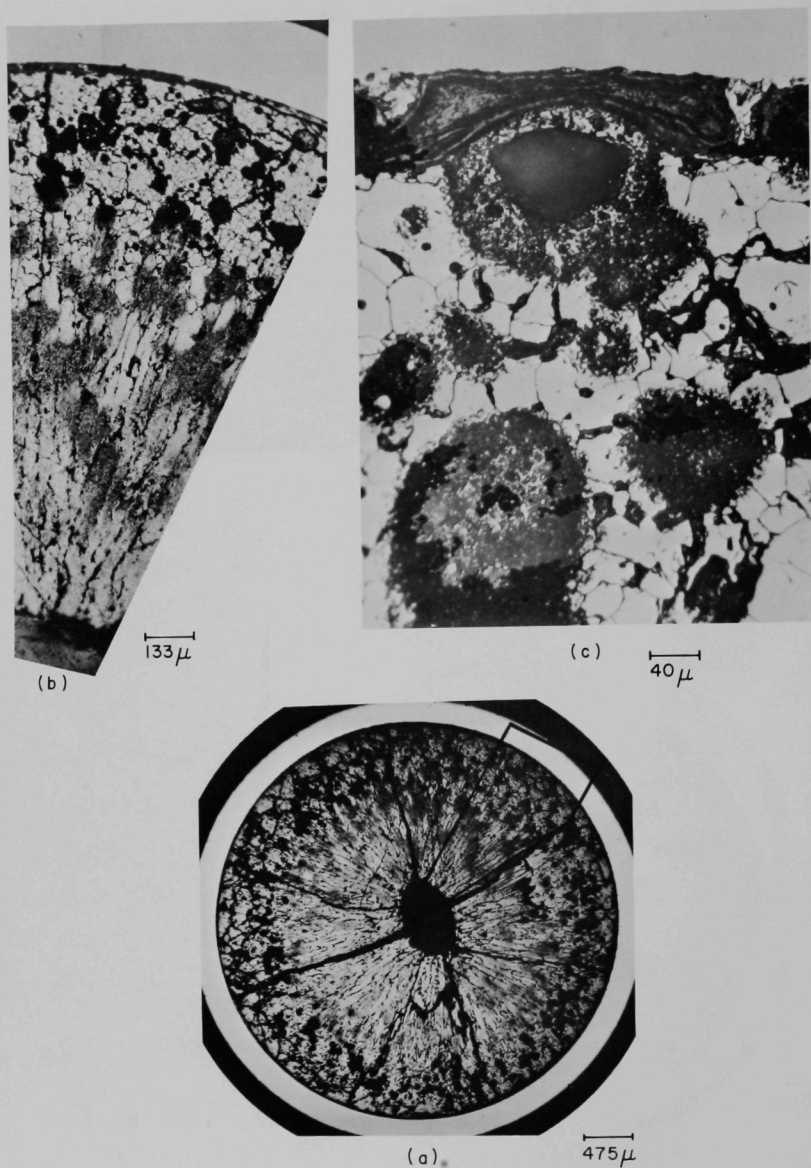
Fig. 24.  Microscopic Views of Radial Cross Section of Sample $D_{4T}$ Taken from Pin 15.  (a) Radial cross section; (b) Enlargement of area indicated on cross section; and (c) Higher enlargement of detail from area, showing porous regions and "bubble" near periphery.
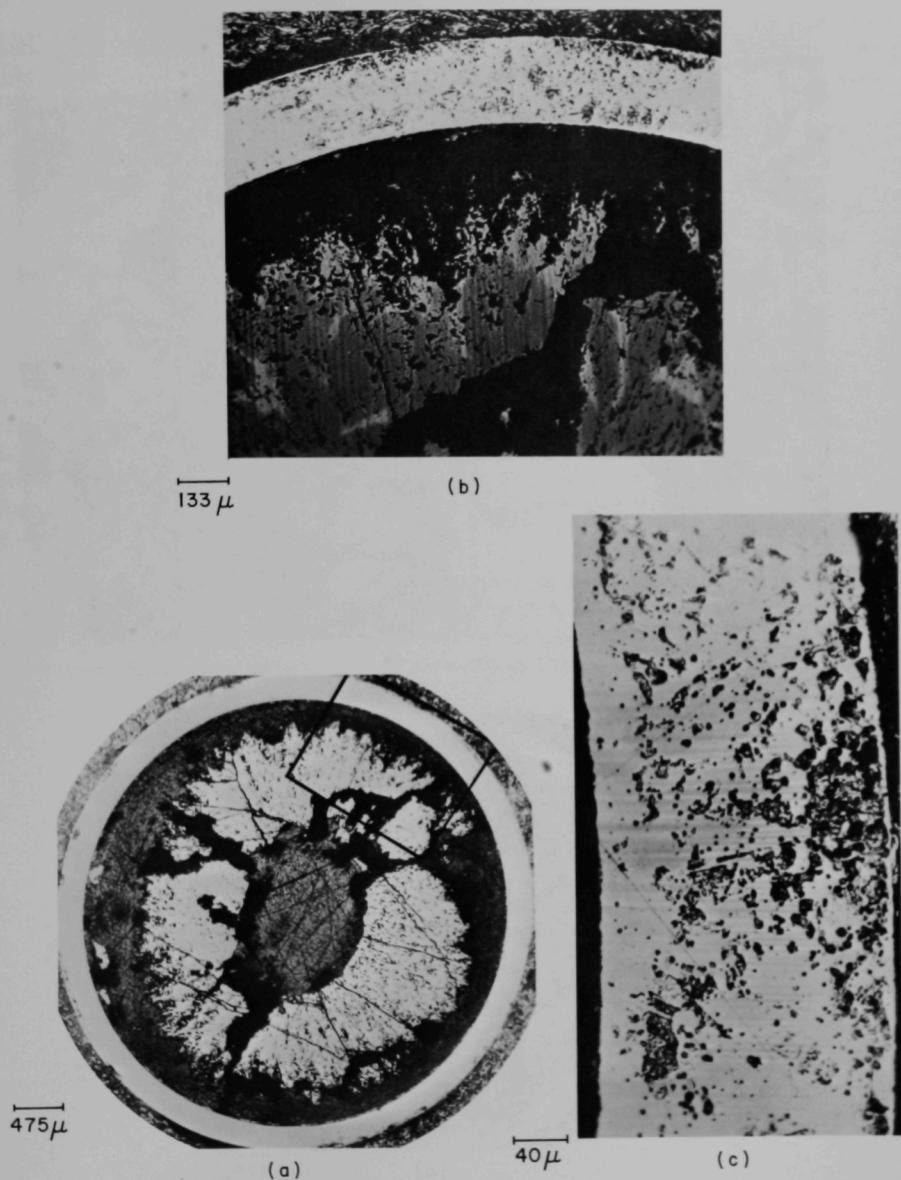
The diametric growth of sample $D_4T$ was 1.46% since its maximum diameter was 0.392 cm and its minimum diameter was 0.381 cm. The central core had a minimum axis of 0.046 cm and a major axis of 0.076 cm. The ratio of the area of the void to the area of the expanded fuel is 2.0%. Annulus measurements yielded values of 0.001 cm for the minor axis and 0.005 cm for the major axis. Figure 24b is a typical core-to-periphery view showing the characteristic grain structure of the various regions. Figure 24c is a further enlargement of a cross section through a bubble at the surface (periphery) of the fuel. These bubbles were a characteristic of all samples examined, varying only in size.

## 10. $D_L$ Samples

Longitudinal samples $D_{1L}$, $D_{2L}$, $D_{3L}$, and $D_{4L}$, taken at pellet interfaces, show the distribution of porous spots along the axis, the peculiar meandering characteristic of the central core, and gross fissures that occur throughout the fuel but are predominantly associated with the central core. Figures 25a, b, and c show samples $D_{1L}$, $D_{3L}$, and $D_{4L}$, respectively. Figure 26a shows sample $D_{2L}$; Fig. 26b is a beta-gamma autoradiograph of sample $D_{2L}$.

Some interesting features visible on Figs. 25 and 26 are, first, the shape and position of the central core, which is indicative of irregularity of the thermal center along the axis of the fuel, and second, the presence of porous areas of segregated high activity in the peripheral areas of the pins.
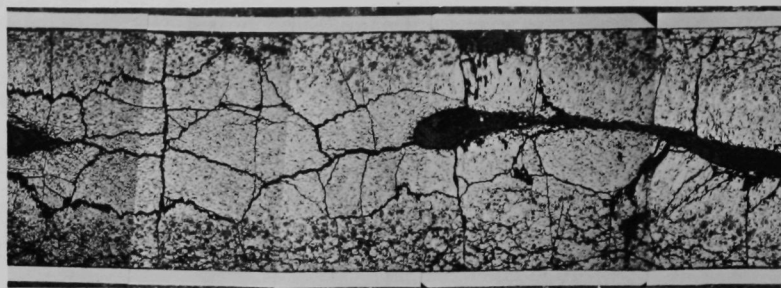
c
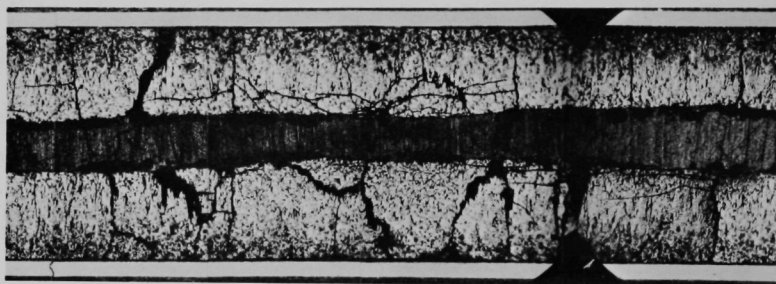


b
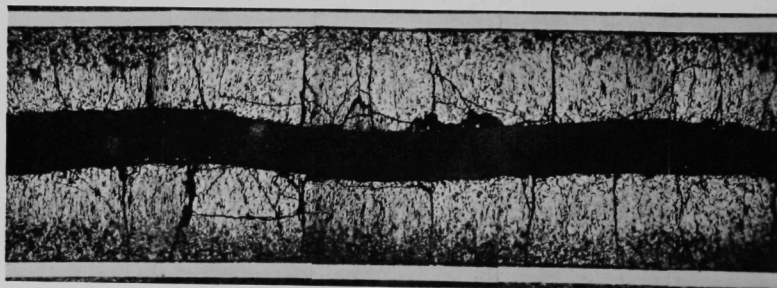


a

112-8901

Fig. 25. Microscopic Views of Longitudinal Sections of Samples $D_{1L}$, $D_{3L}$, and $D_{4L}$ Taken from Pin 15. (a) Longitudinal section of sample $D_{1L}$; (b) Longitudinal section of sample $D_{3L}$; and (c) Longitudinal section of sample $D_{4L}$.
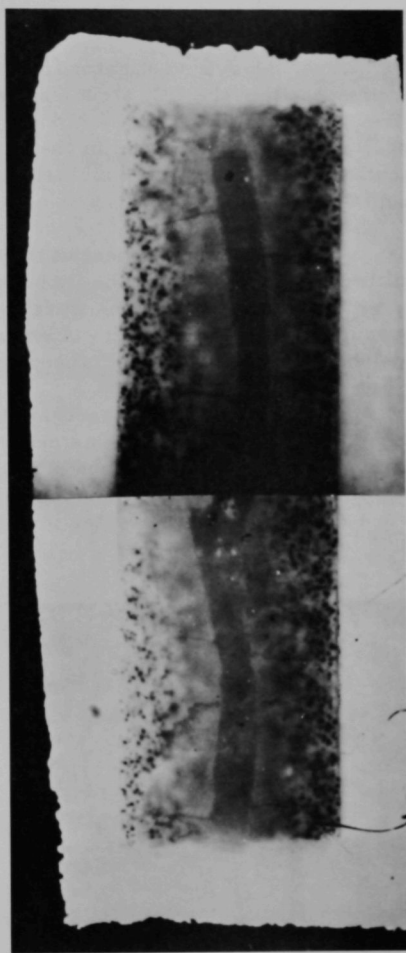
a                                         b

112-8813

Fig. 26. Microscopic Views of Longitudinal Section of Sample $D_{2L}$ Taken from Pin 15. (a) Longitudinal section and (b) Beta-gamma autoradiograph.

## D. Electron-microprobe Examinations

### 1. Introduction

Many investigators have described the retention of fission products within the $UO_2$ structure, and the associated changes in fuel structure, geometry, and composition.[23,25] In addition, the appearance of solid fission-product inclusions in the $UO_2$ has been reported. The microstructural appearance of these inclusions has been reported as being white with a metallic luster.[26,27]

The development of the electron microprobe provided a powerful tool for investigating the inclusions. Solid fission products in the form of white metallic inclusions were identified by this technique, in a 4.6% burnup sample, by Bradbury, Demant, and Marten as the solid elements molybdenum, technitium, ruthenium, and rhodium.[27]

Radial-cross-section photomicrographs of the five control specimens showed white inclusions generally throughout the fuel, but in greater number in the well-developed porous areas. The longitudinal micrographs showed white metallic-appearing inclusions in the form of veins. There were several veins of varying lengths up to 1.0 mm, but all were about 0.02 mm wide.



430 μ

113-1356

Fig. 27. Appearance of Inclusion after 5 months' Storage

The following discussion is divided into two parts: the first, describing preparation of a typical sample; and the second, summarizing the results.

### 2. Typical Sample Preparation

The initial sample was stored for almost 5 months before it was brought back under the microscope for reexamination. During the 5 months' storage, part of the inclusion vein had oxidized, or at least did not possess the same degree of luster as that of the other part. Compare Figs. 9b and c with Fig. 27, and note that the center portion of the inclusion, after 5 months' storage, does not possess the same light-reflecting characteristics as the other portion. Other than this, the sample

was in much the same condition as it had been 5 months earlier. At this stage, the activity of the sample was 8 R/hr/12 in. gamma and 35 R/hr/12 in. beta-gamma.

To be acceptable for the electron-microprobe analysis, the sample had to meet the following requirements:

1. The specimen should have a gamma radiation reading of less than 100 mR/hr/12 in.

2. The sample must be mounted in a copper-impregnated, electrically conductive mount.

3. The mounted sample must be completely free of any loose activity.

The first two requirements mean that our sample had to be de-activated by a factor of 100, and then remounted in an electrically conductive mount.

If the inclusion were a sheet, it would be possible to core-drill a specimen out of the original sample, mount the specimen in a conductive mount upside down, and then approach the inclusion from the rear. But, if the inclusion were not a sheet (and there was some indication that it was a rod), then this approach might require a specimen only 0.0006 in. (0.015 mm) thick. This precision and control are unobtainable with present cave facilities. And even if the degree of control were obtainable, the sample probably could not be handled because of its fragility.

Since close analysis produced evidence that the inclusion could very well be a rod of only 0.02-mm diam, we approached the problem in the following fashion:

1. Core-drill to obtain an approximately 1/16-in.-diam specimen.

2. Monitor activity; if greater than 100 mR/hr/12 in. gamma, proceed to reduce activity level.

3. Mount the $UO_2$ specimen upside down in a gauged brass mount held in by wax.

4. Grind the specimen from the rear until an acceptable activity level is reached.

5. Heat the brass mount to melt the wax and free the specimen.

6. Mount the specimen in a conductive mount.

7. Polish the mounted specimen.

The alignment method used for core drilling was simple but effective. Figure 28a shows how an area was squared off with black plastic electrical tape. The cave operator squared the area off by eye at 6 ft with a manipulator and then carried the sample to the cave stereoscopic microscope for viewing. This trial-and-error method was repeated several times until it was acceptable. The method would have been faster and more precise if the cave had facilities for working under a magnifying viewer.

The drill was a tube of soft brass with 0.157-cm ID and 0.025-cm wall thickness. Buehler $9-\mu$ diamond-polishing compound was used with Hyprez diamond lubricant to cut through the $UO_2$, leaving a 0.127-cm-diam core specimen approximately 0.15 cm long.

Figure 28b shows the hole made by the drilling. Figure 29a shows the apparatus used to core-drill the sample. Figures 29b and c are side and end views, respectively, of the core-drilled specimen.

Immediately after drilling, the specimen was cleaned and its activity level was 3 R/hr/12 in. beta-gamma and 400 mR/hr/12 in. gamma. The drilling had reduced the activity reading a factor of 10, but it still had to be reduced by a factor of 10 again.

We decided to reduce the specimen length in the hope that this operation would reduce the activity to a workable level. To do this, we used a cylindrical brass mount, shown in Fig. 30.

The brass mount was heated by a laboratory hot plate to 120°C with the sample upside down in the center hole. Chunks of a beeswax-rosin mixture, which melts at 60°C, were placed on top of the mount to be melted into all the holes. When the wax was thoroughly melted, the hot mount was placed into a transparent vacuum chamber, which was then evacuated. The air pockets bubbled out and allowed the wax to flow solidly into all the holes and around the specimen. The specimen was made to stay at the bottom of the central hole by gentle pressure from a heated dissecting needle.

The brass-mounted specimen underwent a series of grindings, starting with 180 grit, proceeding to 400 grit, and finishing with 600 grit, until the desired activity level was obtained.

Table X lists the specimen radiation level as monitored by a Juno meter at corresponding thicknesses.

Table X shows that the fourth sample, after having 70% of its thickness ground away, had an activity level a factor of two lower than at the beginning. But between sampling 4 and 5, which represents only a 7% decrease in thickness, the activity level dropped a factor of five. Evidently a "hot spot" had been ground away. This is supporting evidence of the fuel's nonhomogeneity.

(b)

770 μ



(a)

2500 μ
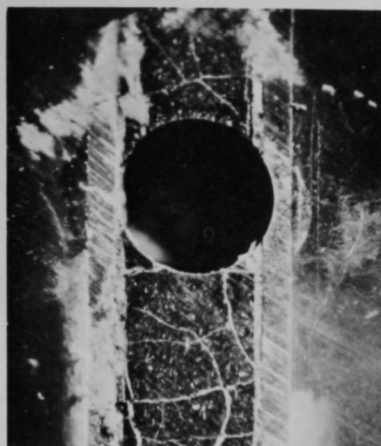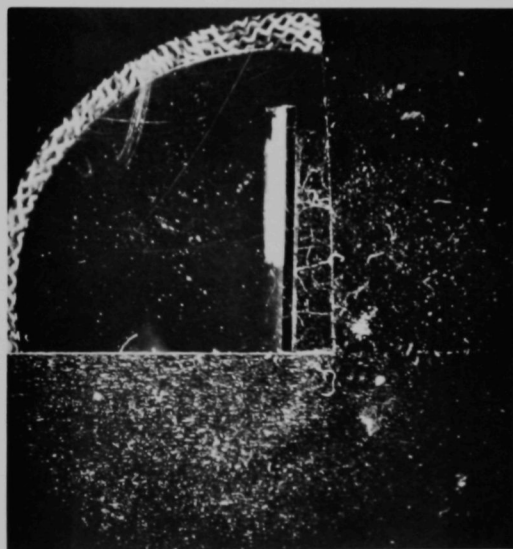
113-1360

Fig. 28. Core Drilling. (a) Alignment and (b) Drilled hole.

770 μ

(b)

770 μ

(c)
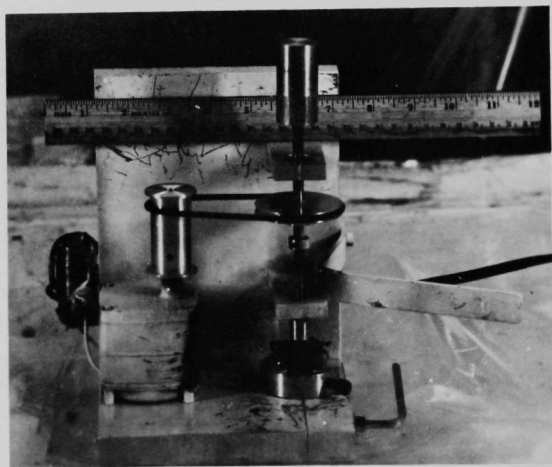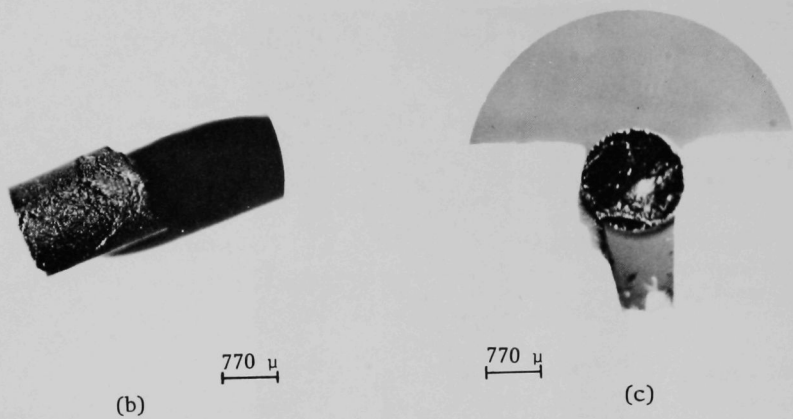


(a)

113-1357

Fig. 29. Drilling Jig and Core-drilled Specimen. (a) Drilling jig; (b) Macroscopic longitudinal view of core; and (c) Macroscopic end view of core.
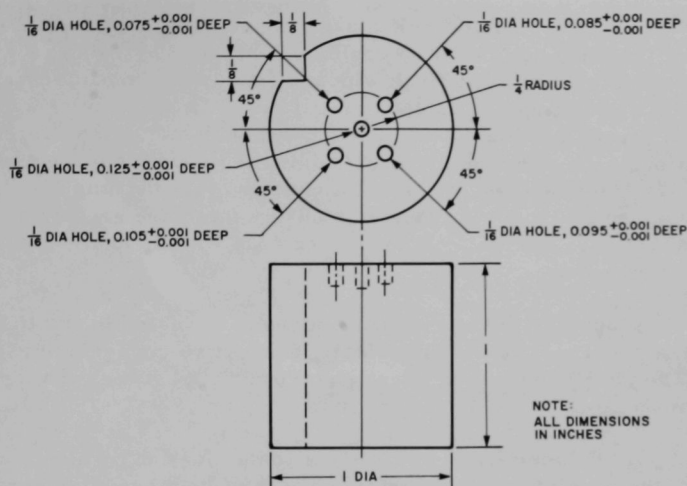
Fig. 30. Cylindrical Brass Mount for Core

TABLE X. Specimen Radiation Level

| Sampling No. | Specimen Thickness, cm | Activity Level |
|---|---|---|
| 1 | 0.165 | 400 mR/hr/12 in. gamma<br>3 R/hr/12 in. beta-gamma |
| 2 | 0.119 | 300 mR/hr/12 in. gamma<br>2 R/hr/12 in. beta-gamma |
| 3 | 0.094 | 300 mR/hr/12 in. gamma<br>2 R/hr/12 in. beta-gamma |
| 4 | 0.050 | 200 mR/hr/12 in. gamma<br>1.8 R/hr/12 in. beta-gamma |
| 5 | 0.038 | 40 mR/hr/12 in. gamma<br>400 mR/hr/12 in. beta-gamma |

Fortunately, the axial position and the size of the "hot spot" were such that the activity could be reduced to an acceptable level of 40 mR/hr/12 in. gamma.

After a thorough cleaning, the brass mount was placed upside down on a hot plate to melt the wax and free the specimen for remounting in a conductive mount.

It was desirable to eliminate any grinding on the final conductive mount, because the inclusion could be destroyed by doing so. Therefore, the specimen had to be flush with the conductive-mount surface to permit only a "touchup" polishing. A tilt of only a fraction of a degree could have caused trouble. After several experiments with different types of tape, along with other methods for holding the specimen to get a satisfactorily flush surface, we found that a coating of Armstrong M-1 grease-viscosity mount lubricant at the specimen-die interface gave repeatedly excellent results. The fuel "touchup" was done with 3- and 1-$\mu$ diamond-polishing compound.

Figure 31 shows the position of the inclusion in the $UO_2$ specimen and its nearness to the electrically conductive copper-impregnated mount. The result was an excellent electrical path between the inclusion and the mount.

After being freed of all loose contamination by ultrasonic washings, the specimen was transferred to the Chemical Engineering Division laboratories for an electron-microprobe analysis.

3.   Electron-microprobe Results

a.   Unirradiated Control Specimen. The apparent heterogeneity of the unirradiated oxide was analyzed, using a control specimen. In addition to the nonhomogeneous distribution of $^{235}U$ (see Fig. 1), small particles of stainless steel up to several microns in diameter were dispersed throughout the fuel material. These steel particles were probably introduced during the mechanical blending process. (Stainless steel mixing blades were used in the blending equipment.)

b.   Microanalysis of Metallic Inclusions. Hundreds of metallic inclusions were analyzed in different areas of the fuel pins. Three general types were found: (1) stainless steel particles; (2) stainless steel particles containing the transition-metal fission products molybdenum, ruthenium, technetium, rhodium, and palladium; and (3) transition-metal fission-product alloys free of stainless steel. These metallic inclusions are discussed below.

(1)   Stainless Steel Inclusions. Small stainless steel inclusions (varying from <1 to 20 $\mu$ in diameter) were found only in the periphery of the fuel matrix and never in the columnar grain-growth region. Larger inclusions were found in many axial and radial cracks as well as in the central void. The latter were probably formed from the stainless steel that was originally near the center of the pin and migrated out of the columnar grain-growth region. In the large inclusions, chromium was frequently depleted or segregated; this would be expected in the higher-temperature region of the fuel.

20 μ                                    (b)

135 μ
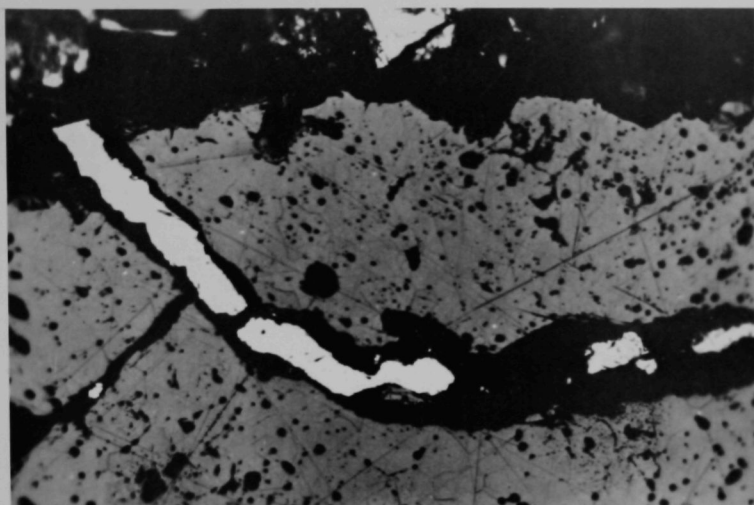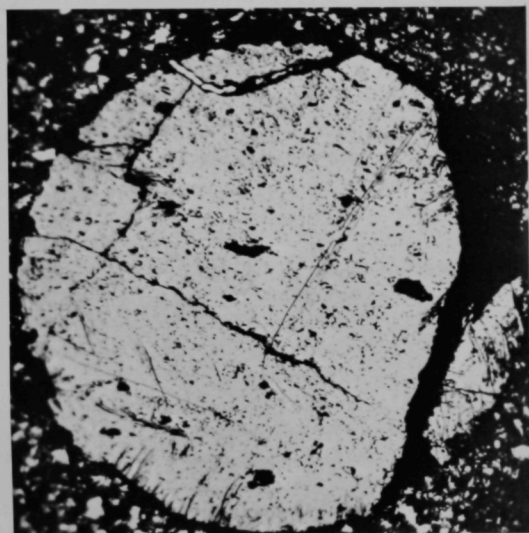
113-1359

Fig. 31. Microscopic Views of Core Mounted in Conductive Mount. (a) Core in conductive
mount and (b) Enlargement of upper portion of core, showing white metallic inclusion.

The distribution of the steel components and uranium for the inclusion shown in Fig. 31 is depicted in Fig. 32, which shows the scanning images obtained with the electron microprobe. Figure 32a is the optical image scanned. Figure 32b is the current image; brightness in the image is inversely proportional to the mean atomic number of the elements present; that is, $UO_2$ appears dark gray, stainless steel appears light gray, and voids appear as white areas. The relative brightness in the X-ray images for iron (Fig. 32c), for nickel (Fig. 32b), for chromium (Fig. 32e), and for uranium (Fig. 32f) are proportional to concentration. The concentration of chromium in this image varied from 3 to 4 w/o in the main portion of the inclusion to almost 100 w/o in the chromium-rich regions of the inclusion. Average concentrations of iron and nickel in this inclusion were 78 and 18 w/o, respectively.

(2) Stainless Steel Inclusions Containing Transition-metal Fission Products. These inclusions were always found within the large porous regions at the periphery of the pins. A few were found in the matrix outside the columnar grain-growth region, particularly in the low-burnup sample (0.75 a/o), where the large porous areas were not well defined and in areas near the columnar grain-growth region. There was no consistent ratio of fission-product distribution in the steel-containing inclusions, although molybdenum and ruthenium were usually the major fission products. In several instances, the steel inclusions contained large amounts of palladium and no other fission products.

(3) Transition-metal Fission-product Inclusions Free of Stainless Steel. These inclusions, which contained molybdenum, ruthenium, technetium, and rhodium, but no stainless steel, were found only in the region of columnar grain growth. Quantitative analysis of inclusions greater than 1 $\mu$ in diameter showed them to be free of uranium, indicating that no intermetallics or solid solutions of uranium-transition metal fission products were formed. The inclusions smaller than 1 $\mu$ in diameter could not be quantitatively analyzed because the electron-diffusion volume in the sample resulted in an X-ray production zone larger than the actual inclusion volume. However, by estimating the composition of the smaller particles, we showed that they were also free of uranium. We made this estimate by comparing the total X-ray intensity (corrected for detector and excitation efficiency) of all the transition-metal fission products, as a function of the inclusion diameter, with the total X-ray intensity produced in an inclusion of the size of the effective X-ray production diameter. The results indicated that the total counts of transition-metal X rays agreed quite well with the counts estimated from the size of the inclusion. The effective X-ray production diameter was estimated by analyzing successively-smaller inclusions until the total X-ray production (corrected for detector and excitation efficiency) dropped off from a constant value. The electron beam was focused to less than 0.25 $\mu$ in diameter, and under the experimental conditions, the effective X-ray production diameter of the inclusions was
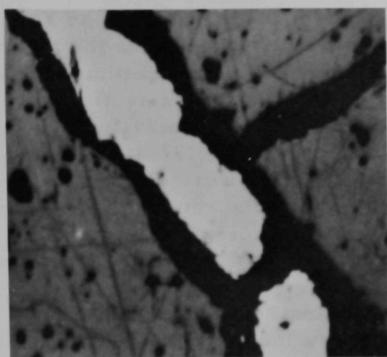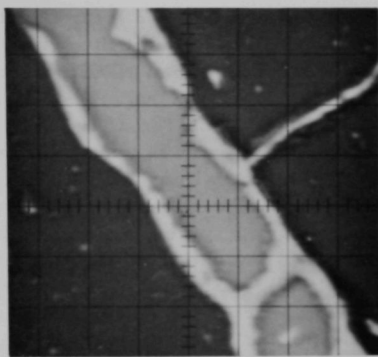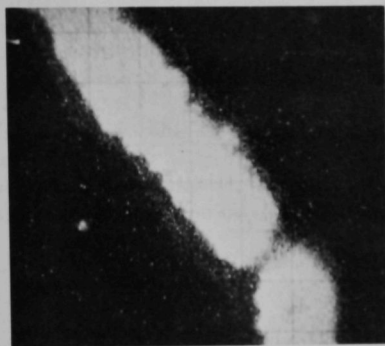
113-1358    (e)                            (f)

Fig. 32. Enlarged Portion of Inclusion Shown in Fig. 31 (900X). (a) Optical image; (b) Specimen current image; (c) Iron Kα X-ray image; (d) Nickel Kα X-ray image; (e) Chromium Kα X-ray image; and (f) Uranium Mβ X-ray image.
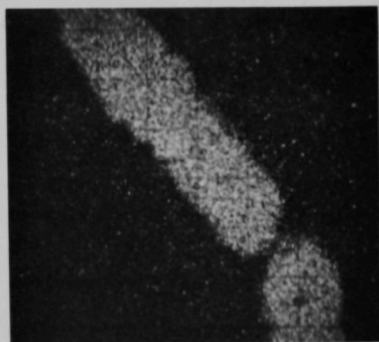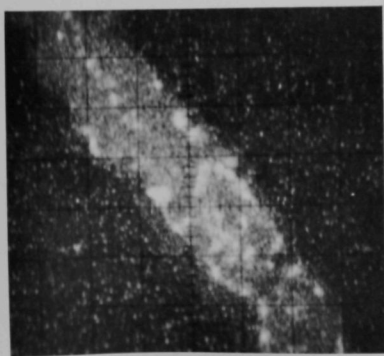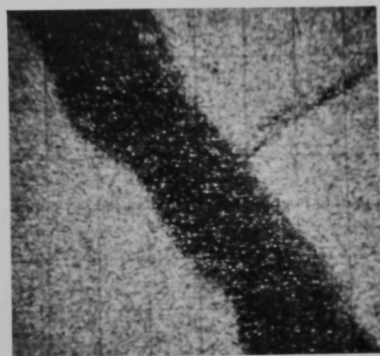
approximately 1.0 to 1.2 $\mu$ for this diameter beam. Figure 33, an X-ray spectral profile of one of the larger inclusions, demonstrates the absence of uranium. More than 100 inclusions of this type were quantitatively analyzed as a function of radial position in all the transverse sections. Figures 34 and 35 show the compositional variation of the inclusions in the columnar grain-growth region of the bottom of pin 8 (4.37 a/o burnup) as a function of radial position. Similar distributions were obtained in the other cross sections analyzed. Figure 34 shows the actual concentrations* of molybdenum, ruthenium, technetium and rhodium in each inclusion. The preferential migration of one fission product to another can be seen more readily in Fig. 35, where the ruthenium-molybdenum, technetium-molybdenum, rhodium-molybdenum, technetium-ruthenium, rhodium-ruthenium, and rhodium-technetium weight ratios are given as functions of radial position. The solid lines in the figures represent the theoretical concentrations or weight ratios based on the best fission-yield data available. The analyses of all the inclusions were based on the assumption that the sum of the weight fractions of the individual transition-metal fission products was unity. Whenever the inclusion analyzed was smaller than the effective X-ray production zone, the data were corrected accordingly.

c. <u>Microanalysis of Large Porous Inclusions</u>. Large porous inclusions up to 100 $\mu$ in diameter were formed in the peripheral region of the fuel pins beyond the columnar grain-growth region. These areas correspond to the areas of high activity in beta-gamma autoradiographs.
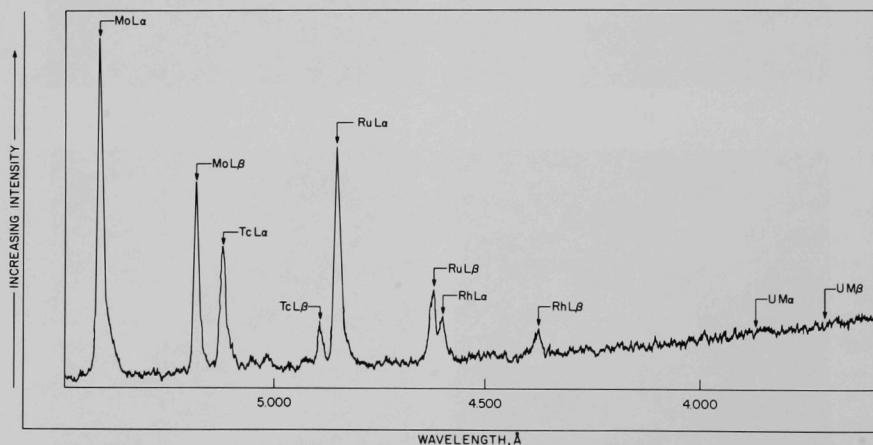


308-1302

Fig. 33. X-ray Intensity Scan of Inclusion in Columnar Grain-growth Region of Irradiated UO$_2$, Showing the Presence of Molybdenum, Technetium, Ruthenium, and Rhodium, and the Absence of Uranium

*The measured concentrations (w/o) were derived from the observed intensity ratio of the sample to that of the pure element; no corrections were made for absorption, fluorescence, or atomic-number effects.
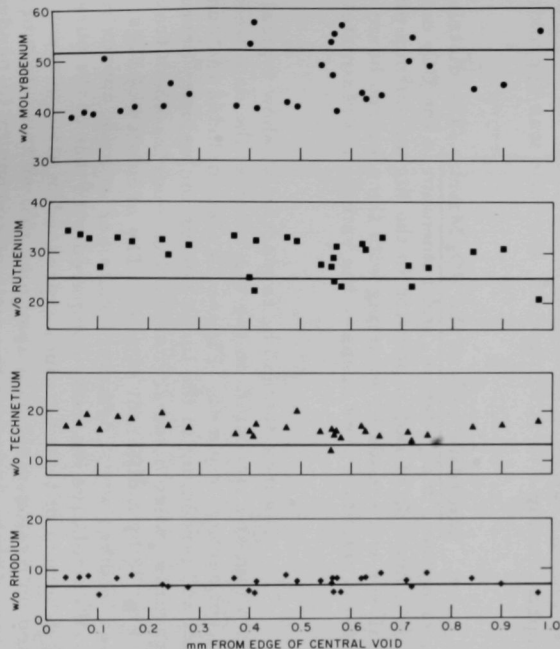
308-1305

Fig. 34. Concentrations (in w/o) of Transition-metal Fission
Products in Metal Inclusions Located in Columnar
Grain-growth Region of Irradiated UO$_2$ Fuel Pin
(bottom section of pin 8). Solid lines indicate the-
oretical concentrations based on fission yields.
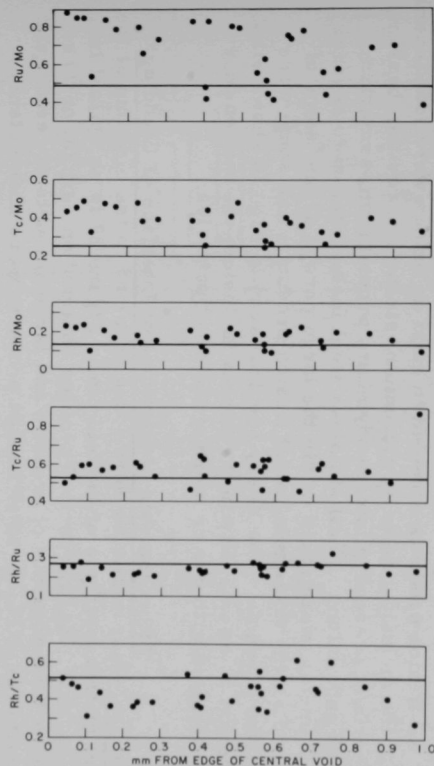
308-1304

Fig. 35. Weight Ratios of Transition-metal Fission Products in
Metal Inclusions Located in Columnar Grain-growth
Regions of Irradiated UO$_2$ Fuel Pin (bottom section of
pin 8). Solid lines indicate theoretical concentrations
based on fission yields.

Electron-microprobe analyses verified that these were regions of high enrichment, and thus of high burnup. Several inclusions were analyzed qualitatively for all the fission products by scanning over a 45-$\mu$-square area with the electron beam. Figure 36 is an X-ray spectral scan of one of these inclusions. All fission products expected to exist as oxides were found evenly distributed in the inclusion, namely, zirconium, strontium, cesium, barium, lanthanum, cerium, praseodymium, neodymium, promethium, samarium, europium, and gadolinium. Small stainless steel inclusions, up to several microns in diameter, were found within the large porous areas; some of these contained all the transition-metal fission products, and some were devoid of fission products. The X-ray spectral scan in Fig. 36 shows silicon to be present as an impurity in the porous inclusion; the silicon may have been associated with one or more of the steel particles.

d. Microanalysis of Particles at Interface of Cladding and Fuel Matrix. Many particles were found adhering to the cladding at the cladding-fuel matrix interface of the fuel pins. Figure 37 is an optical image of a typical particle. X-ray spectral profiles obtained on several of these particles showed the presence of uranium and large amounts of cesium and barium (probably as oxides); other fission products were undetectable. Small stainless steel inclusions were sometimes imbedded within these particles and appear as shiny white areas in the figure. The ratio of cesium concentration (w/o) in the particles at the interface of the cladding and the fuel matrix to the concentration of cesium in one of the large porous inclusions was approximately 5 to 1; for barium, the ratio was approximately 2.5 to 1.

e. Microanalysis of the $UO_2$ Matrix. The distributions of neodymium, zirconium, molybdenum, and ruthenium in the $UO_2$ matrix were determined as a function of radial position in the higher-burnup pins (pins 8 and 15). Analyses were made by scanning with the electron beam and integrating the X-ray intensity over areas of the sample approximately 10 or 20 $\mu$ square.

Figures 38a and b, respectively, show typical distributions of neodymium and zirconium in the $UO_2$ matrix; the data were obtained from the bottom section of pin 15. Figure 38 also includes the concentrations of neodymium and zirconium in the large porous inclusions. Several different radial traverses were made across the $UO_2$ matrix. Each traverse is indicated in Fig. 38 by a different symbol. The ordinates of Figs. 38a and b are expressed in three ways, namely, counts per second, approximate weight percent (based on relative intensity compared with that of the pure element), and equivalent burnup of total uranium expressed in atom percent. The latter value is based on fission-yield data assuming that no migration of the fission product occurs. Figure 38c gives the ratio of zirconium-to-neodymium count rates as a function of radial position. The theoretical ratio of the zirconium-to-neodymium count rates calculated from fission-yield data, detector
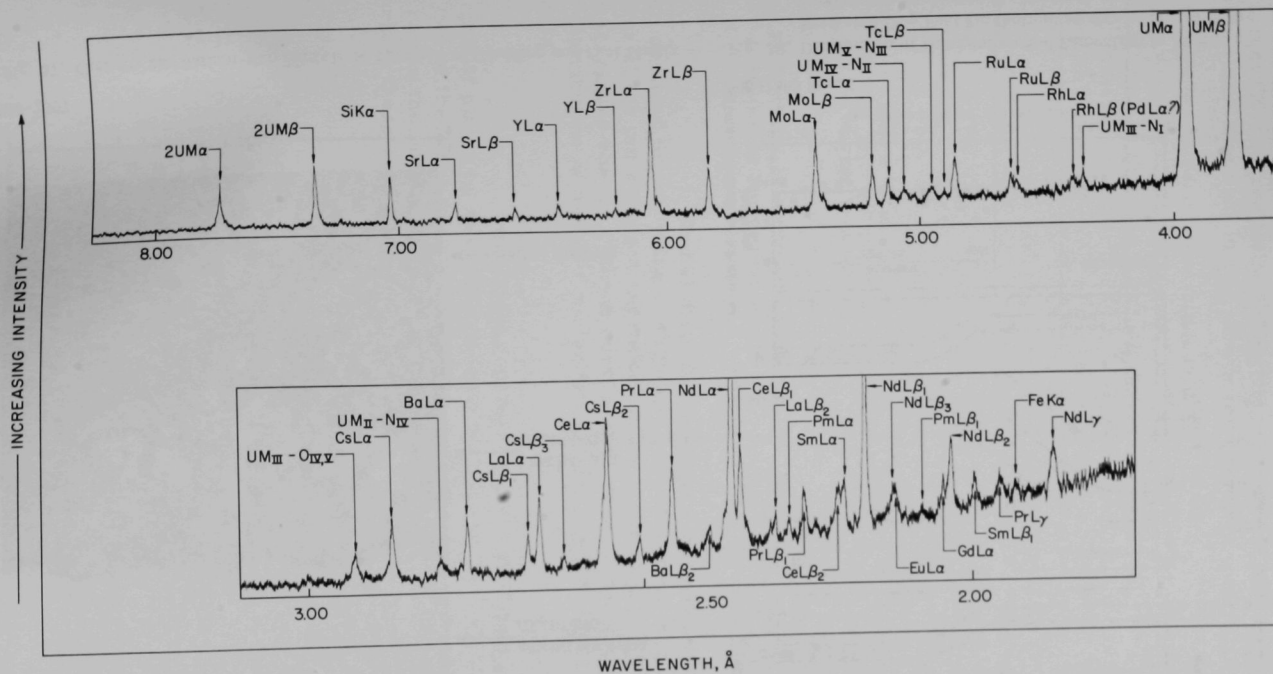
Fig. 36. X-ray Intensity Profile Scan of Large Porous Inclusion in Irradiated $UO_2$ Fuel Pin
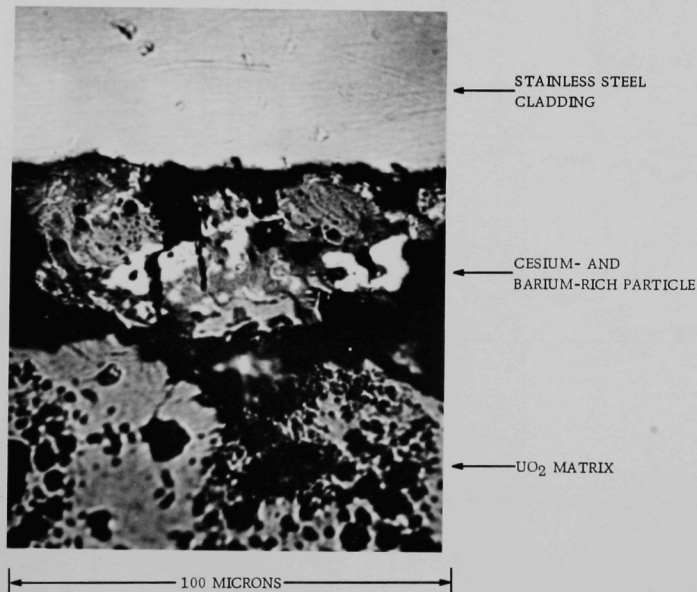
308-1301

308-1307

Fig. 37. Cesium- and Barium-rich Particle at Interface of Cladding and Fuel Matrix
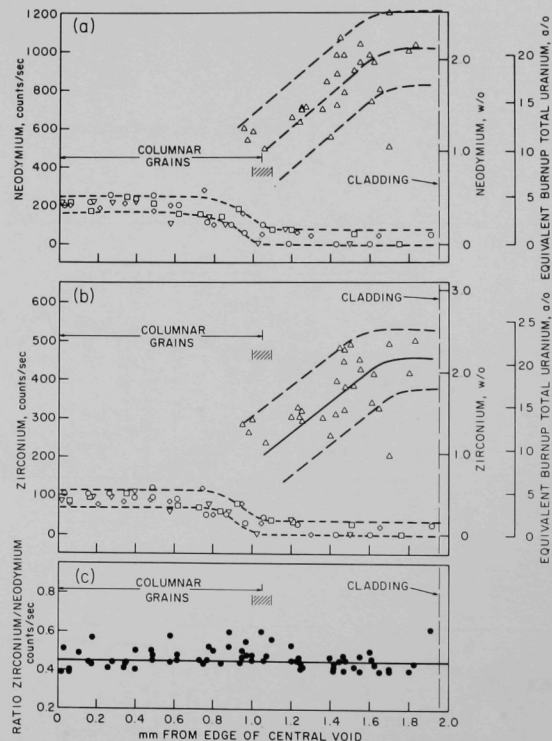


308-1303 Rev. 1

Fig. 38. Distribution of Neodymium and Zirconium in Matrix of Irradiated $UO_2$ Fuel Pin (bottom section of pin 15; 6 a/o burnup). Symbols are: $\triangle$, concentrations in porous inclusions; $\bigcirc$, $\square$, $\diamondsuit$, $\triangledown$, concentrations in different radial traverses of $UO_2$ matrix; $\bullet$, X-ray intensity ratios in all areas analyzed.

efficiency, X-ray excitation efficiency, and matrix absorption is shown as a solid line. The data in Fig. 38c agree quite well with the theoretical value, showing no preferential migration of zirconium in relation to neodymium.



Figure 39 shows the distribution of molybdenum and ruthenium in the matrix, as a function of radial position in the top section of pin 15. Analyses were made in small areas (10 $\mu$ square) of the $UO_2$ matrix in the columnar grain region where no inclusions were present. The concentration (uncorrected for matrix effects) of molybdenum in the matrix was 0.26 ± 0.03 w/o, and ruthenium was undetectable (<0.008 w/o).

308-1300

Fig. 39. Distribution of Molybdenum and Ruthenium in Matrix of Irradiated $UO_2$ Fuel Pin (top section of pin 15; 6 a/o burnup)

Radial distribution curves for molybdenum and ruthenium obtained by analyzing contiguous areas 50 $\mu$ square across the entire radius of the pin were not reproducible from one radial traverse to another. The irregular shapes of these curves were greatly influenced by the irregular distribution of metallic inclusions and large porous inclusions within the matrix.

Plutonium concentrations were determined in the top portion of pin 15 by analyzing several portions of the $UO_2$ matrix as well as two of the large porous inclusions. Analyses showed a depletion of plutonium in the porous inclusions with respect to the matrix. Table XI summarizes these results.

TABLE XI. Plutonium Concentrations in
Top Section of Pin 15

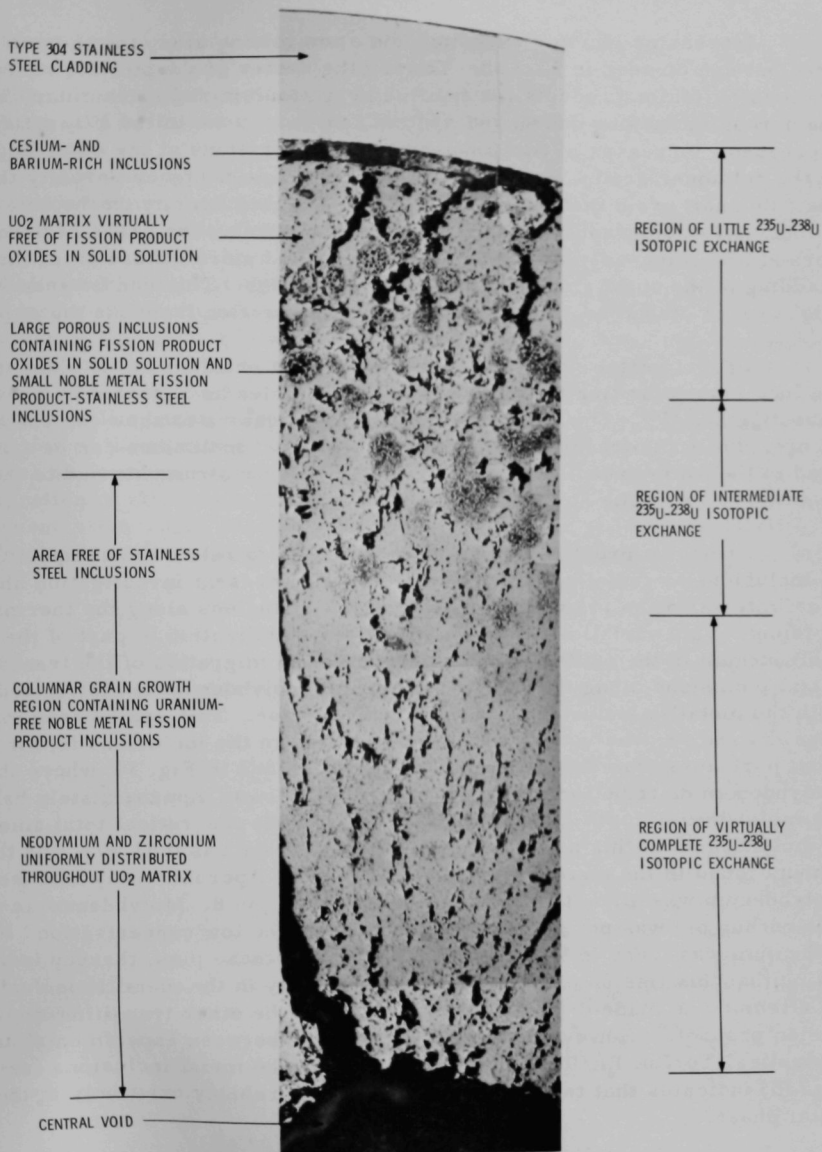| Type of Area | Distance from Central Void Edge, mm | Plutonium, w/o |
|---|---|---|
| Porous | 1.03 | 0.53 |
| Porous | 1.15 | 0.60 |
| Matrix | 0.03 | 0.77 |
| Matrix | 0.37 | 0.76 |
| Matrix | 0.71 | 0.78 |
| Matrix | 0.98 | 0.81 |

## III. DISCUSSION

Figure 40 shows the general features typical of the microprobe specimens. The stainless steel particles present in the original fuel material were probably introduced during the mechanical blending process of fully enriched and depleted $UO_2$ particles to obtain the 13% enrichment.

The temperatures in the center of the fuel pins, including the columnar grain regions, were hot enough to melt the steel particles and expel them from the columnar grains. Molten steel filled many of the radial and axial cracks in the cooler outer sections of the pins. In addition, large amounts of steel were sometimes found at the inner edge of the central void at radial cracks, suggesting that some of the steel ejected from the columnar grains flowed down radial cracks into the central void of the pin. Apparently, most of the steel was ejected from the columnar-grain region before any significant amount of fission took place, since the transition-metal fission products (molybdenum, ruthenium, technetium, rhodium, and palladium) were undetectable in any of the large steel inclusions, either in the radial or axial cracks or in the central void. Steel particles that were in the molten state in cooler sections of the pin (in the large porous inclusions or in the equiaxial grains just outside the columnar grain region) served as getters for the transition-metal fission products. Some sort of selective zone refining or selective extraction apparently took place in the outer edge of the pins, because some steel inclusions contained large amounts of palladium as the only gettered fission product and others contained primarily molybdenum and ruthenium.

The preparation of the 13% enriched $UO_2$ fuel material (mechanical blending and subsequent sintering) did not provide appreciable isotopic exchange of $^{235}U$ and $^{238}U$, as evidenced by the beta-gamma autoradiograph of the original fuel material in Fig. 1. However, during irradiation, the central areas of the pins, including most of the columnar-grain-growth regions, were hot enough to provide relatively complete isotopic exchange of the $^{235}U$ and $^{238}U$. This was shown by a relatively uniform density in beta-gamma autoradiographs as well as by the fairly uniform distribution of neodymium and zirconium in the oxide matrix in these areas (see Fig. 40).

In the outer region, little isotopic exchange of uranium took place. The porous inclusions (Fig. 40) were approximately the same size as the original fully enriched $UO_2$; this was verified by a real analysis of the outer area, which showed that the porous areas comprised about 10-15% of the total area. Plutonium formed from $^{238}U$, which was of uniform concentration in the $UO_2$ matrix, was depleted in the porous areas. Few, if any, fission products were seen in the matrix adjacent to the porous inclusions. Equivalent burnup of greater than 20 a/o was reached in some of the inclusions, a burnup that is considerably higher than the total overall enrichment of $^{235}U$. The large amount of porosity can be attributed to fission-gas production.

TYPE 304 STAINLESS STEEL CLADDING

CESIUM- AND BARIUM-RICH INCLUSIONS

$UO_2$ MATRIX VIRTUALLY FREE OF FISSION PRODUCT OXIDES IN SOLID SOLUTION

LARGE POROUS INCLUSIONS CONTAINING FISSION PRODUCT OXIDES IN SOLID SOLUTION AND SMALL NOBLE METAL FISSION PRODUCT-STAINLESS STEEL INCLUSIONS

AREA FREE OF STAINLESS STEEL INCLUSIONS

COLUMNAR GRAIN GROWTH REGION CONTAINING URANIUM-FREE NOBLE METAL FISSION PRODUCT INCLUSIONS

NEODYMIUM AND ZIRCONIUM UNIFORMLY DISTRIBUTED THROUGHOUT $UO_2$ MATRIX

CENTRAL VOID

REGION OF LITTLE $^{235}U$-$^{238}U$ ISOTOPIC EXCHANGE

REGION OF INTERMEDIATE $^{235}U$-$^{238}U$ ISOTOPIC EXCHANGE

REGION OF VIRTUALLY COMPLETE $^{235}U$-$^{238}U$ ISOTOPIC EXCHANGE

308-1310 Rev. 2

Fig. 40. Enlarged Area Extending from Central Void to Cladding (middle section of pin 15) Showing Typical Structural Features Identified by Electron-microprobe Analysis

Increasing isotopic exchange and atom mixing along the thermal gradient can be seen in Fig. 38. Toward the center of the pin, the concentrations of fission products (as typified by zirconium and neodymium) in the porous inclusions decreased and the concentrations in the $UO_2$ matrix increased. Increases of fission-product concentrations at the outer edge of the columnar grains were associated with areas of higher porosity than the columnar-grain matrix and with areas of higher density on the beta-gamma autoradiographs. Etched sections showed that the areas of porosity caused by fission-gas release became larger and more diffuse from the cladding to the outer region of the columnar grains. This can be seen in Fig. 24b, an etched segment from a transverse section from the top of pin 15.

Experimental evidence for the absence of uranium in the shiny metallic inclusions clarifies the nature of these particles as reported by previous investigators.[26-29] The inability of these investigators to show the absence of uranium in the transition-metal fission-product inclusions can be attributed to the lower takeoff angle for X rays in their instruments and to the inability to focus the electron beam to less than $0.25 \mu$.

Previous investigators made no attempts to relate the composition of inclusions to radial position in the fuel. The present investigation shows a definite variation in the composition of the inclusions along the thermal gradient. This variation is influenced by the stabilization of part of the molybdenum in the oxide phase as well as by the migration of the transition-metal inclusions along the thermal gradient. Molybdenum is distributed in both the metallic inclusions and in the oxide phase. This can be seen in Figs. 34 and 35, where the molybdenum content in the inclusions is, for the most part, less than the theoretical yield value, and in Fig. 39, where the molybdenum distribution in the $UO_2$ matrix is shown. Approximately half the molybdenum in pin 15 is in the $UO_2$ matrix; the theoretical total amount of molybdenum in this pin based on fission-yield data is 0.53 w/o, and the amount found in the matrix was $0.26 \pm 0.03$ w/o. Approximately half the molybdenum was also stabilized in the matrix of pin 8. Molybdenum in the low-burnup pin was not determined, because of the low concentration. No ruthenium was found in the $UO_2$ matrix of any of these pins, thereby indicating that this fission product is distributed only in the metallic inclusions. No attempt was made to analyze the matrix for the other transition-metal fission products. However, the good agreement between experimental and theoretical Tc/Ru, Rh/Ru, and Rh/Tc ratios in the metal inclusions (see Fig. 35) indicates that technetium and rhodium probably exist only in the metal phase.

Electron-probe analyses show a definite migration of the transition-metal fission-product inclusions along the thermal gradient. The inclusions were not evenly distributed across the radius of the pins. Total analyses for molybdenum and ruthenium in contiguous large areas, including the $UO_2$ matrix and the inclusions, showed that the concentrations of these

elements in the columnar-grain region were below those predicted from fission-yield data and were higher than the predicted values at the juncture of the columnar and equiaxed grains. Any trend in the peripheral regions was masked by the irregular distribution of the $^{235}U$-rich inclusions.

Insufficient data have been obtained to postulate with certainty the direction and mechanism of migration of metallic inclusions. The frequent thermal cycling of test reactors such as MTR and the presence of numerous stainless steel inclusions add to the uncertainty involved in proposing a definite mechanism at this time. However, some of the experimental data suggest movement of the inclusions toward the cooler end of the thermal gradient. Whenever two or more metallic inclusions were analyzed in the same columnar grain, a buildup of molybdenum with respect to the other fission products was seen at the hotter edge. This can readily be explained if the metallic inclusions were moving toward the cooler zone. A major fraction of the fission product molybdenum comes from 65-day $^{95}Zr$, which forms an immobile oxide. (It has been impossible to detect any significant migration of zirconium in any of the pins studied.) Thus, the molybdenum concentration would gradually build up in the areas away from the direction of mobility of the metallic species as zirconium decayed into molybdenum.

## ACKNOWLEDGMENTS

## REFERENCES

1. C. E. Dickerman, *Experiments and Analyses in Fast Reactor Safety*, Nucl. Safety *8*(3), 220 (1967).

2. C. E. Dickerman, L. E. Robinson, W. Doe, and R. Stewart, "Properties of Irradiated $UO_2$ Pins Prior to Transient Reactor Test (TREAT) Facility Transients," in *Reactor Physics Division Annual Report, July 1, 1965 to June 30, 1966*, ANL-7210, Paper IV-4.

3. R. R. Stewart, C. E. Dickerman, W. Doe, and N. Stalica, "Properties of 6 a/o Burnup Oxide Fast Reactor Fuel Pins Prior to Transient Reactor Test (TREAT) Facility Exposure," in *Reactor Physics Division Annual Report, July 1, 1966 to June 30, 1967*, ANL-7310, Paper IV-4.

4. C. E. Dickerman, L. E. Robinson, and R. Stewart, *Photographic TREAT Fast Reactor Safety Experiments on Irradiated Oxide Pins*, Trans. Amer. Nucl. Soc. *9*(2), p. 396 (1966).

5. C. E. Dickerman and R. R. Stewart, "Results from Transient Reactor Test (TREAT) Facility Fast Reactor Oxide Fuel Pin," in *Reactor Physics Division Annual Report, July 1, 1966 to June 30, 1967*, ANL-7310, Paper IV-5.

6. R. R. Stewart, C. E. Dickerman, L. E. Robinson, and W. B. Doe, *Studies of Fast Reactor Fuel Element Behavior Under Transient Heating to Failure. III. In-pile Experiments on Irradiated $UO_2$ Fuel Pins in the Absence of Coolant*, ANL-7552 (March 1969).

7. D. E. White, Metallurgy Division, ANL, private communication.

8. Reactor Handbook, *Materials*, Vol. I, Interscience Publishers, New York (1964), p. 293.

9. B. D. Holt and D. Pettis, Chemistry Division, ANL, private communication.

10. R. Bene and A. M. Essling, Chemistry Division, ANL, private communication.

11. R. J. Meyer, Chemical Engineering Division, ANL, private communication.

12. D. R. Huff, Chemistry Division, ANL, private communication.

13. J. H. Monaweck and E. S. Sowa, *Summary Report on Irradiation of Prototype EBR-II Fuel Elements*, ANL-6010 (Sept 1960).

14. H. Berger and W. J. McGonnagle, *Progress Report on Neutron Radiography*, ANL-6279 (1962).

15. R. J. Armani, Reactor Physics Division, ANL, private communication.

16. R. P. Larsen, Chemical Engineering Division, ANL, private communication.

17. S. Katcoff, *Fission-Product Yields from Neutron-Induced Fission*, Nucleonics *18*(11), 201 (1960).

18. L. J. Templin, Ed., *Reactor Physics Constants*, ANL-5800 (2nd Ed.) pp. 4-6 (July 1963).

19. A. B. Cohen, Reactor Physics Division, ANL, private communication.

20. W. B. Lewis, *Engineering for the Fission Gas in $UO_2$ Fuel*, Nucl. Appl. *2*, 171 (1966).

21. C. E. Dickerman, L. E. Robinson, E. S. Sowa, and S. B. Skladzien, *Studies of Fast Reactor Fuel Element Behavior Under Transient Heating to Failure. II. In-pile Experiments on UO2 Samples in the Absence of Coolant*, ANL-6845 (Jan 1965).

22. T. J. Pashos, D. R. deHalas, D. L. Keller, and L. A. Neimark, "Irradiation Behavior of Ceramic Fuels," in *Proc. Third U.N. International Conf. on Peaceful Uses of Atomic Energy, Geneva, 1964*, Vol. 11, p. 472, U.N., New York (1965).

23. J. Belle, Ed., *Uranium Dioxide: Properties and Nuclear Applications*, Naval Reactor Handbook Series, USAEC (1961), pp. 593-610.

24. J. E. Cunningham, R. J. Beaver, and R. C. Waugh, "Fuel Dispersion in Stainless Steel Components for Power Reactors," in *Fuel Elements Conference, Paris*, TID-7546 (March 1958), pp. 243-268.

25. B. Lustman, *Engineering Effects of Radiation on Materials*, Vol. 2, Special Technical Publication 220, Philadelphia, ASTM (1957).

26. B. T. Bradbury, J. T. Demant, *et al.*, *Electron Probe Microanalysis of Irradiated UO2*, J. Nucl. Mater. *17*(3), 227, 1965.

27. B. T. Bradbury, J. T. Demant, and P. M. Marten, *Solid Fission Products in Irradiated Uranium Dioxide*, AERE-R-5149, United Kingdom Atomic Energy Authority, Harwell Berkshire, 7 (1966).

28. B. T. Bradbury, J. T. Demant, P. M. Marten, and D. M. Poole, *Electron Probe Microanalysis of Irradiated UO2*, AERE-R-4845 (1965).

29. B. M. Jeffery, *Microanalysis of Inclusions in Irradiated UO2*, J. Nucl. Mater. *22*, 33 (1967).